

Hot corino chemistry in the Class I binary source Ser-emb 11

RAFAEL MARTÍN-DOMÉNECH,¹ JENNIFER B. BERGNER,^{2,3} KARIN I. ÖBERG,¹ JOHN CARPENTER,⁴ CHARLES J. LAW,¹
JANE HUANG,^{5,3} JES K. JØRGENSEN,⁶ KAMBER SCHWARZ,⁷ AND DAVID J. WILNER¹

¹*Center for Astrophysics | Harvard & Smithsonian
60 Garden St., Cambridge, MA 02138, USA*

²*University of Chicago Department of the Geophysical Sciences, Chicago, IL 60637, USA*

³*NHFP Sagan Fellow*

⁴*Joint ALMA Observatory, Alonso de Córdova 3107 Vitacura, Santiago, Chile*

⁵*Department of Astronomy, 8 University of Michigan, 323 West Hall, 1085 S. University Avenue, Ann Arbor, MI 48109, USA*

⁶*Niels Bohr Institute & Centre for Star and Planet Formation, University of Copenhagen
Øster Voldgade 5-7, DK-1350 Copenhagen K*

⁷*Lunar and Planetary Laboratory, University of Arizona, Tucson, AZ 85721, USA*

(Received; Revised; Accepted)

Submitted to ApJ

ABSTRACT

We report the detection of more than 120 emission lines corresponding to 8 complex organic molecules (CH₃OH, CH₃CH₂OH, CH₃OCH₃, CH₃OCHO, CH₃COCH₃, NH₂CHO, CH₂DCN, and CH₃CH₂CN) and 3 isotopologues (CH₂DOH, ¹³CH₃CN, and CH₃C¹⁵N) toward the western component of the Ser-emb 11 binary young stellar object (YSO) using observations with the Atacama Large Millimeter/submillimeter Array at ~1 mm. The complex organic emission was unresolved with a ~0.5'' beam (~220 au) in a compact region around the central protostar, and a population diagram analysis revealed excitation temperatures above 100 K for all COMs, indicating the presence of a hot corino. The estimated column densities were in the range of 10¹⁷ – 10¹⁸ cm⁻² for the O-bearing COMs, and three orders of magnitude lower for the N-bearing species. We also report the detection of H₂CO and CH₃OH emission in a nearby millimeter source that had not been previously catalogued. Ser-emb 11 is classified in the literature as a Class I source near the Class 0/I cutoff. The estimated COM relative abundances in Ser-emb 11 W and the other three Class I hot corino sources reported in the literature are consistent with those of Class 0 hot corinos, suggesting a continuity in the chemical composition of hot corinos during protostellar evolution.

1. INTRODUCTION

Complex (6+ atoms) organic molecules (COMs), the precursors of yet more complex prebiotic species, are thought to be formed in space by energetic processing of interstellar ice mantles and/or by gas-phase reactions following ice sublimation (Herbst & van Dishoeck 2009). During the star-formation process, COMs can be incorporated into protostellar and protoplanetary disk structures (Öberg & Bergin 2020), where they could be preserved in small bodies such as comets (see, e.g., Altwegg et al. 2016) and eventually delivered to nascent planets,

perhaps triggering a prebiotic chemistry on their surfaces.

In the interstellar medium (ISM), COMs were first detected in the gas phase of hot (T ~ 300 K) and dense (n_H ≥ 10⁶ cm³) regions around high-mass protostars, so-called hot cores (e.g., Ball et al. 1970; Solomon et al. 1971; Rubin et al. 1971; Blake et al. 1987; Turner 1991; Charnley et al. 1992). Later on, detection of COMs was also reported toward a number of Class 0 and a few Class I low-mass protostars (e.g., Cazaux et al. 2003; Arce et al. 2008; Öberg et al. 2010; Bianchi et al. 2019a). Those Class 0 and Class I sources where COMs have been detected in a warm (T ≥ 100 K) and compact (~100 au) region around the central protostar are known as hot corinos, in analogy to the hot cores around high-mass protostars. There is an increased interest in Class I

hot corinos in particular, since evidence of early planet formation have been found in Class I and borderline Class I/II sources (ALMA Partnership 2015; Harsono et al. 2018; Sheehan & Eisner 2018; Tychoniec et al. 2020; Segura-Cox et al. 2020)

Table 1 lists the Class 0 and Class I sources with reported hot corino chemistry in the literature, according to the above definition (COMs at $T > 100$ K detected within ~ 100 au of the central object). Eight hot corinos had been detected as of the year 2018. This number doubled in the following two years, with the addition of seven confirmed sources, and four hot corino candidates (G211.47-19.27S, G208.68-19.20N1, G210.49-19.79W, G192.12-11.10, Hsu et al. 2020, not included in Table 1). In addition, there are a number of recent interferometric surveys dedicated to a systematic study of the presence of organic chemistry at planet-forming scales in samples of Class 0/I sources, such as FAUST (Bianchi et al. 2020), CALYPSO (Belloche et al. 2020), and PEACHES (Yang et al. 2021). The PEACHES survey recently identified 15 additional Class 0 sources with compact emission of CH_3OH and at least one other COM, consistent with the presence of a hot corino (Yang et al. 2021). However, since the COM excitation temperatures were not constrained in half of these sources, we have not included them in Table 1.

Of the 15 hot corino sources listed in Table 1, only three (SVS13-A, Ser-emb 17, and L1551-IRS5) are Class I YSOs ($70 \text{ K} < T_{bol} < 650 \text{ K}$), while the rest are classified as Class 0 ($T_{bol} < 70 \text{ K}$). Class I sources represent the evolutionary link between the young Class 0 sources, deeply embedded in their parental dense envelopes, and the more evolved Class II/III YSOs, where most of the envelope has dissipated. It is currently unclear how (and if) the organic chemistry evolves between the Class 0 and Class I evolutionary stages. In particular, the small number of detected Class I hot corino sources, along with the large scatter in COM abundances measured toward Class 0 hot corinos (see, e.g., Bergner et al. 2019; Belloche et al. 2020), make it hard to evaluate whether the complex organic chemistry changes during the protostellar phase.

In the cases when the hot corino chemistry is detected in binary protostellar systems at either the Class 0 (IRAS 16293-2422, IRAS 4A) or Class I (SVS13-A, and L1551-IRS5) stages, the comparison of the complex organic content observed toward the two components yield mixed results. In IRAS 16293-2422 and L1551-IRS5, both components appeared to harbor hot corino chemistry (Jørgensen et al. 2011; Bianchi et al. 2020), while the COM emission detected in IRAS 4A and SVS13-A had been mostly associated with the IRAS 4A2 and

Table 1. Hot corino sources reported in the literature.

Source	Class ^a	Binary?	Reference
IRAS 16293	0	y	Cazaux et al. (2003)
IRAS 4A	0	y	Bottinelli et al. (2004)
IRAS 2A	0	n	Jørgensen et al. (2005)
IRAS 4B	0	n	Bottinelli et al. (2007)
HH 212	0	n	Codella et al. (2016)
B335	0	n	Imai et al. (2016)
L483	0	n	Oya et al. (2017)
B1-bS	0	n	Lefloch et al. (2018)
SVS13-A	I	y	Bianchi et al. (2019a)
Ser-emb 1	0	n	Martin-Domenech et al. (2019)
Ser-emb 8	0	n	Bergner et al. (2019)
Ser-emb 17	I	n	Bergner et al. (2019)
L1551-IRS5	I	y	Bianchi et al. (2020)
BHR 71 IRS1	0	n	Yang et al. (2020)
B1-c	0	n	van Gelder et al. (2020)

NOTE—^aBased on T_{bol} from André et al. (2000); Enoch et al. (2009); Pezzuto et al. (2012); Green et al. (2013); Tobin et al. (2016)

VLA4A components, respectively (López-Sepulcre et al. 2017; Bianchi et al. 2019a, and ref. therein). These findings were somewhat puzzling, since the chemical composition in binary sources might be expected to be similar across the different components, as they should be shaped by the same initial conditions of the parental molecular cloud. It is currently unclear whether this observed chemical differentiation is due to differences in the physical conditions of the individual sources, different evolutionary stages of the individual sources, or differences in the dust opacity toward the two components that could hinder the COM detection in one of them (Sahu et al. 2019; Belloche et al. 2020; De Simone et al. 2020).

In this work, we report the serendipitous detection and characterization of hot corino chemistry toward Ser-emb 11 W. Ser-emb 11 is a binary source where the west component was proposed to harbor a massive disk of $0.13 M_{\odot}$ (Enoch et al. 2011). This source is located in Cluster B of the Serpens Molecular Cloud, a star-forming cloud at a distance of $d = 436 \pm 9$ pc (Ortiz-León et al. 2018) that harbors 34 embedded protostars (9 Class 0 and 25 Class I sources) identified in Enoch et al. (2009). Ser-emb 11 was classified as a Class I source in Enoch et al. (2009) according to its bolometric temperature of $T_{bol} = 77$ K. Since this temperature is close to the Class 0/I cutoff (70 K, André et al. 2000), Ser-emb 11 could also be seen as a transitional source between the

Class 0 and Class I stages. If we adopt the classification in Enoch et al. (2009), Ser-emb 11 W constitutes the fourth hot corino detected toward a Class I source to date. We also report the presence of complex organic chemistry toward a nearby millimeter source that had not been previously catalogued.

In this paper, the observations are described in Sect. 2, along with the calibration and imaging processes. An overview of the Ser-emb 11 source is presented in Sect. 3.1. The complex molecule detections toward the Ser-emb 11 W component are presented in Sect. 3.2, and characterized in Sections 3.3–3.5. Sect. 3.6 is dedicated to the smaller molecules also observed toward this source. Sect. 3.7 presents evidence consistent with the presence of a protostellar disk in Ser-emb 11 W. The organic chemistry detected toward the additional millimeter source is presented in Sect. 3.8. The results are discussed in Sect. 4, and the conclusions are summarized in Sect. 5.

2. OBSERVATIONS

This work is based on observational data from an ALMA project aiming at systematically characterizing the chemistry in disks at different evolutionary stages (#2015.1.00964.S). This project has previously led to the detection of hot corino chemistry in two Class 0 and one Class I sources in the Serpens Molecular Cloud (Ser-emb 1, 8, and 17, Martin-Domenech et al. 2019; Bergner et al. 2019). The observations analyzed in this paper were completed during Cycle 3 using two different Band 6 frequency settings, and were centered on Ser-emb 17 ($R.A._{J2000} = 18\text{h } 29\text{m } 06.20\text{s}$, $Dec_{J2000} = +00^{\circ} 30' 43.1''$). The characterization of the emission detected toward Ser-emb 17 was presented in Bergner et al. (2019, 2020). Figure 1 shows the 1.3 mm continuum emission map of a $26'' \times 26''$ region around Ser-emb 17. Emission from the Ser-emb 11 source and another millimeter source that we have named Ser-emb ALMA 1 (Sect. 3.8) was also observed within the half power beam width of the primary beam (HPBW $\sim 26''$).

The majority of the data presented here correspond to two broad spectral windows of 1.875 GHz bandwidth observed with a native spectral resolution of 1.19–1.25 km/s. These spectral windows spanned 231.481–233.356 GHz and 242.978–244.853 GHz, and covered a large number of COM transitions. In addition, a series of 14 narrow spectral windows spread across 217–233 GHz and 243–262 GHz, with bandwidths between 58.6 MHz and 117.2 MHz and a native spectral resolution of 0.16 – 0.20 km/s, were also observed. These narrow spectral windows targeted particular transitions of simpler O-, C-, N-, and S-bearing

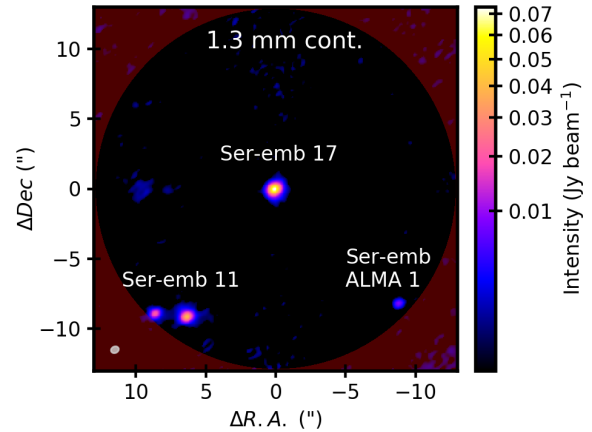


Figure 1. 232 GHz continuum emission of the Ser-emb 17 and Ser-emb 11 sources, and an additional millimeter source not classified in the literature that we have named Ser-emb ALMA 1 (Sect. 3.8). The map is clipped at 2σ ($\sigma = 0.35$ mJy beam $^{-1}$). The size of the synthesized beam is shown on the lower left corner. The three sources were observed within the same field of view, centered at Ser-emb 17. The region of the field of view observed outside the half power beam width of the primary beam is colored in red.

species, namely, SiO, CO, ^{13}CO , C^{18}O , H_2CO , C_2H , $c\text{-C}_3\text{H}_2$, N_2D^+ , DCN, H^{13}CN , HC^{15}N , and CS. A list of the observed spectral windows can be found in Table 3 of Appendix A. The observations of the first frequency setting (217–233 GHz) were carried out on June 05 and 14, 2016, using 42 antennas (longest baseline of 772.8 m) for a total on source time of 19.2 min. The second frequency setting (243–262 GHz) was observed on May 15 and 16, 2016, using 41 antennas (longest baseline of 640.0 m) for a total on source time of 22.5 min.

2.1. Calibration of the observed visibilities

The observed visibilities were initially calibrated by ALMA staff with the Common Astronomy Software Applications (CASA) versions 4.5.3 and 4.7.0, using the sources J1751+0939, J1830+0619 as bandpass and phase calibrators, respectively, and Titan as the absolute flux calibrator. In order to work with manageable datasets, the calibrated visibilities centered on the Ser-emb 17 source were split into four separate measurement sets containing the lower and upper sideband visibilities of the two frequency settings. Four continuum measurement sets were generated from the channel-averaged visibilities of all spectral windows in each sideband after flagging channels containing line emission. One round of phase self-calibration was then performed in CASA 5.4.1 using these continuum datasets. For that purpose, the continuum visibilities were imaged using the task `tclean` with Briggs weighting of the

baselines (robustness parameter = 0.5) and the Hogbom deconvolver. The polarization-independent (gain-type = T), self-calibration phase solutions were subsequently obtained with the task `gaincal`, and applied to the continuum-subtracted, native resolution visibilities. Continuum subtraction had been previously performed in the uv plane using line-free channels. The self-calibration process led to an increase of 4–12% in the peak intensity of the continuum images, and a decrease of 6–22% in the corresponding rms. Finally, the continuum-subtracted, self-calibrated visibilities corresponding to the different spectral windows were further split into different measurement sets before their imaging.

2.2. Imaging of the calibrated visibilities

Imaging of the continuum-subtracted, self-calibrated visibilities was performed with CASA version 5.4.2, using the task `tclean` with Briggs weighting of the baselines (robustness parameter = 0.5) down to a $\sim 2\sigma$ noise threshold, with $\sigma \sim 3.0$ mJy beam $^{-1}$ for the two 1.875 GHz bandwidth spectral windows, and $\sigma \sim 7.5$ mJy beam $^{-1}$ for the narrow spectral windows. The corresponding σ was estimated as the average rms over ten line-free channels of a $8''$ diameter region that included (but was not centered on) the Ser-emb 11 source. The two 1.875 GHz bandwidth spectral windows were imaged with a uniform channel width of 0.63 km/s, while the narrow spectral windows were imaged with a channel width of 0.14 – 0.17 km/s (corresponding to their native channel spacing). A multi-scale deconvolver with default values (`scales` = 0, 5, 15; `smallscalebias` = 0.6) was used in order to account for both compact and extended emission. During the imaging process, an auto-mask was applied independently to every channel of the self-calibrated visibilities, using the default parameters for auto-masking line emission: `sidelobethreshold` = $2.0 \times \text{rms}$, `noisethreshold` = $4.25 \times \text{rms}$, `lownoisethreshold` = $1.5 \times \text{rms}$, `minbeamfrac` = 0.3, and `negativethreshold` = 15.0. The size of the resulting synthesized beam is listed in Table 3 of Appendix A. The average synthesized beam for the two 1.875 GHz bandwidth spectral windows was $0.57'' \times 0.47''$ (PA $\sim -66^\circ$). We applied the primary beam correction to all images. This was of particular importance for this work since both analyzed sources were close to the edge of the half power beam width, with primary beam correction factors of ~ 0.5 – 0.6 .

CASA version 5.5.0 was used to compute the moment 0 maps of individual transitions integrating the detected emission over the full line width of every emission line. The moment 0 rms for each transition was measured in

a $8''$ diameter region after integration of the same number of line-free channels as the corresponding moment 0 map. The rms values were in the 5–18 mJy beam $^{-1}$ km s $^{-1}$ range in all cases, except for the CO moment 0 map, with $\sigma \sim 40$ mJy beam $^{-1}$ km s $^{-1}$. This is likely the result of the CO moment 0 map having $\sim 5\times$ more channels than the rest.

The spectra at the pixels corresponding to the continuum peaks of the Ser-emb 11 binary source (pixel size = $0.08''$) were extracted assuming a source velocity of 8.5 km/s as a first approximation. The rms of the spectra was measured using the Python function `numpy.std` to calculate the observed standard deviation in six line-free regions of the spectra. An average value of $\sigma \sim 4$ mJy beam $^{-1}$ was found.

3. RESULTS

3.1. Overview of the Ser-emb 11 binary source

Figure 2 presents an overview of the Ser-emb 11 binary source, as traced by millimeter continuum emission, and CO, C 18 O, H $_2$ CO, and CH $_3$ OH line emission. These species are good tracers of the outflows (CO), envelope (C 18 O), and complex organic chemistry (CH $_3$ OH) in YSOs. H $_2$ CO is a COM precursor, and thus traces the complex organic chemistry, but it is also a good tracer of the outflows and protostellar envelopes (Tychoniec et al. 2021). The continuum map shown in the left panel was generated by combining all line-free channels in the 1.875 GHz bandwidth spectral window centered at ~ 232 GHz. The continuum map rms was 0.35 mJy beam $^{-1}$. The continuum emission peaks were used to identify the position of the Ser-emb 11 E and Ser-emb 11 W central protostars, marked in every panel of Fig. 2.

The CO $J = 2-1$ moment 0 map is shown in the second panel of Fig. 2 and presents a brighter emission toward the continuum peak of Ser-emb 11 W compared to Ser-emb 11 E. The extended emission detected toward the east of Ser-emb 11 E and the north-west of Ser-emb 11 W may be tracing outflows in the east to west (E-W) and the north-west to south-east (NW-SE) directions, driven by Ser-emb 11 E and Ser-emb 11 W, respectively. Additional information on the possible outflows is presented in Appendix E. The negative contours in the second panel of Fig. 2 result from incomplete flux recovery and spatial filtering upon the interferometric imaging of extended emission (note that the maximum recoverable scale of the observations was $10''$).

The C 18 O $J = 2-1$ emission (third panel of Fig. 2), a good tracer of the protostar envelopes, presents a similar peak intensity toward the Ser-emb 11 E and W components. It also includes a extended component around

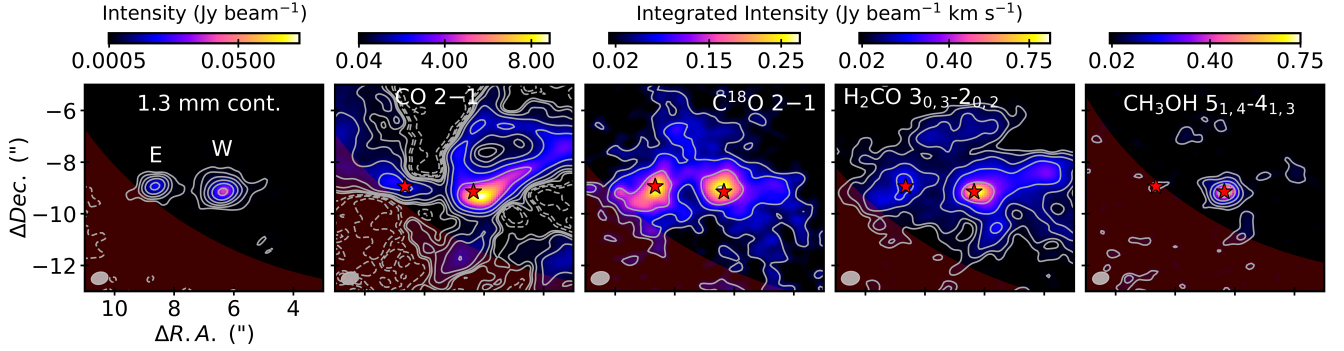


Figure 2. 232 GHz continuum, and CO, C¹⁸O, H₂CO, and CH₃OH integrated line emission maps toward Ser-emb 11 E and Ser-emb 11 W, along with the 3, 6, 12, 24, 48, and 96 σ contours in white (solid lines), and -3, -6, -12, -24, -48, and -96 σ contours (dashed lines, see the text). The x and y axes indicate the offset with respect to the center of the observations (Ser-emb 17). The positions of the continuum emission peaks are marked with a star symbol in each panel. Maps are clipped at 1 σ . The size of the synthesized beam is shown on the lower left corner of each panel. The region of the field of view observed outside the half power beam width of the primary beam is colored in red.

both protostars, suggesting that they have similar gas envelopes.

Line emission from the COM precursor H₂CO (fourth panel of Fig. 2) is detected toward both protostars, and presents also an extended component, but it is a factor of ~ 4 brighter toward Ser-emb 11 W. On the other hand, CH₃OH (5_{1,4} – 4_{1,3}) emission was only detected in a compact, marginally resolved region toward the continuum peak of Ser-emb 11 W. This suggests that the western component of the binary system could harbor hot corino chemistry. The hot corino nature of Ser-emb 11 W is further evaluated in the following Sections.

3.2. Detection of organic molecules toward Ser-emb 11 W

The spectra at the continuum peak of Ser-emb 11 E and Ser-emb 11 W in the 231.262 GHz – 233.380 GHz range and the 242.978 GHz – 244.853 GHz range are presented in Fig. 3 (top three panels and bottom three panels, respectively). While no transitions were observed toward Ser-emb 11 E in this spectral range, more than 120 lines were identified toward Ser-emb 11 W. In order to assign the emission lines, we used the Spectral Line Identification and Modelling (SLIM) module within the MADCUBA¹ package (Martín et al. 2019), which makes use of the Jet Propulsion Laboratory (JPL; Pickett et al. 1998) and the Cologne Database for Molecular Spectroscopy (CDMS; Müller et al. 2005) spectral catalogs. To confirm the assignments, the SLIM module allowed us to simultaneously identify all detectable

transitions of a particular species in our spectral range. A list of the identified molecular transitions in Fig. 3 is presented in Tables 4–8 of Appendix B. The detected species presented multiple emission lines in our spectral range that were observed with a signal-to-noise ratio (SNR) higher than 3 ($\sigma \sim 4$ mJy, Section 2.2). Additional tentatively detected lines (observed with SNR < 3) corresponding to these species are also indicated in Fig. 3 and listed in Appendix B, but they were not considered in the following discussion. Species with only one line observed at SNR > 3 were considered tentative detections.

A total of five O-bearing COMs were detected toward the continuum peak of Ser-emb 11 W: CH₃OH, CH₃CH₂OH, CH₃OCH₃, CH₃OCHO, and CH₃COCH₃, along with the CH₂DOH isotopologue (Tables 4-7). Two emission lines tentatively assigned to CH₂CO and t-HCOOH are also included in Table 4. Table 8 lists the observed emission lines corresponding to three confirmed N-bearing COMs (NH₂CHO, CH₂DCN, and CH₃CH₂CN), and the ¹³CH₃CN and CH₃C¹⁵N isotopologues, as well as one tentatively detected N-bearing species (HNCO). Three emission lines corresponding to small (4 atoms or less) S-bearing species are also identified in Fig. 3. They are presented in Sect. 3.6 along with the additional small molecules detected in dedicated, narrow spectral windows.

3.3. COM spatial distribution in Ser-emb 11 W

In order to explore the spatial distributions of the different O- and N-bearing COMs detected toward Ser-emb 11 W, Fig. 4 presents the moment 0 maps of the strongest observed transitions of every species among those with $E_{up} > 75$ K (highlighted in Tables 4-8 of Appendix B). Unblended emission lines were preferen-

¹ The MADrid Data CUBe Analysis package is a software developed at the Center of Astrobiology (Madrid, INTA-CSIC) to visualize and analyze single spectra and data cubes (Rivilla et al. 2016, 2017).

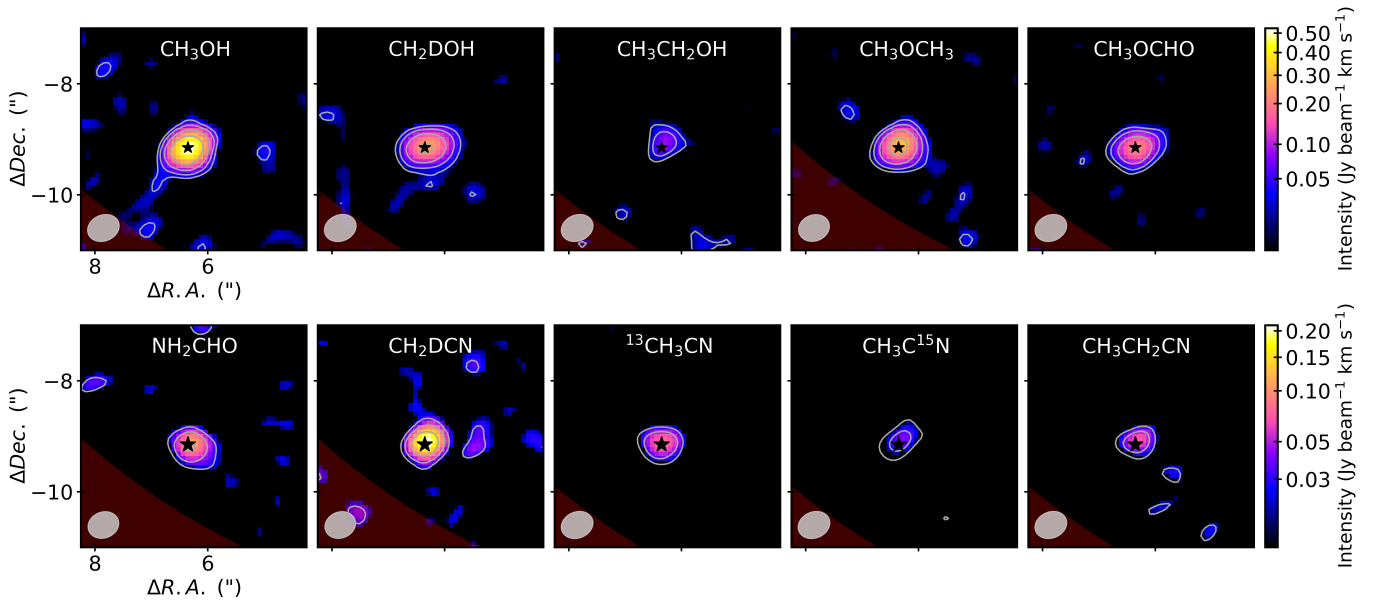


Figure 4. Integrated moment 0 maps toward Ser-emb 11 W, along with the 3, 6, 12, and 24σ contours, of the O-bearing (top panels) and N-bearing (bottom panels) COM transitions highlighted in Tables 4-8 of Appendix B. The position of the continuum emission peak is marked with a star symbol in each panel. Maps are clipped at 2σ . The size of the synthesized beam is shown on the lower left corner of every panel. The region of the field of view observed outside the half power beam width of the primary beam is colored in red.

tially selected. CH_3COCH_3 is not included in Fig. 4, since its emission lines were not strong enough to adequately image them. In all cases, the emission of the organic molecules appears unresolved in a compact region around the central protostar.

We estimated the size of the emitting region observed for the CH_3OH ($10_{3,7} - 11_{2,9}$) line (the strongest unblended COM emission line with $E_{up} > 75$ K, top left panel of Fig. 4), using a 2D Gaussian fit in CASA. After deconvolving the synthesized beam, the resulting estimated size was $\Omega_{source} = 0.17'' \times 0.11''$ (74 au \times 48 au). We assumed this emission size for all COMs throughout the rest of the paper, although the actual size could be smaller.

Assuming that the unresolved COM emission corresponds to a hot corino, and that COMs were sublimated from the ice mantles upon passive heating of the inner envelope, we can calculate the expected size of the hot corino based on the protostellar radial temperature profile:

$$T(r) = 60 \left(\frac{r}{1.34 \times 10^4 \text{ au}} \right)^{-q} \left(\frac{L_{bol}}{10^5 L_{\odot}} \right)^{q/2} \text{ K}, \quad (1)$$

with $q = 2/(4+\beta)$ (Chandler & Richer 2000). Assuming $\beta = 1.5$ (Bergner et al. 2019) and $L_{bol} = 4.8 L_{\odot}$ (Enoch et al. 2011), the estimated radial distance at which the temperature drops below 100 K (the desorption temperature of a water-rich ice mantle) is ~ 24 au. This corresponds to a source size (diameter) of $\Omega_{100K} \sim 0.11'' \times 0.11''$ (diameter), which is only a factor of ~ 1.5 smaller than our adopted emission region.

3.4. COM excitation temperatures and column densities in Ser-emb 11 W

For those COMs with detected transitions spanning a wide range of upper level energies ($\Delta E_{up} \gtrsim 150$ K), a population diagram analysis was used to derive excitation temperatures and column densities from the observed line integrated intensities. The analysis was adopted from Goldsmith & Langer (1999) and is described in Appendix C. The line integrated intensities ($\int S_{\nu} dv$) and uncertainties were calculated by fitting a Gaussian to the spectral features observed in Fig. 3, using the Levenberg-Marquardt minimization implementation of `scipy.optimize.curve_fit` in Python. In the case of multiple blended transitions, a multiple Gaussian fitting approach was adopted. More information about the fitting process can be found in Appendix B. The estimated position, width, integrated intensities, and uncertainties of the identified emission lines are listed in Tables 4–8. The average full width half maximum

(FWHM) of the O- and N-bearing COM emission lines was 3.0 – 3.5 km/s. CH_3OH and NH_2CHO presented broader emission lines (FWHM ~ 4.2 km/s), while the CH_3OCHO lines were slightly narrower (~ 2.7 km/s).

Figures 5 and 6 present the population diagrams of the detected O-bearing and N-bearing COMs, respectively. The upper level populations (N_u) are corrected according to Eq. C5 using the corresponding optical depth correction factor (C_{τ}) and a filling factor ($\Omega_{beam}/\Omega_{source}$) of 14.3, according to the deconvolved size of the CH_3OH emitting region in Sect. 3.3 (and assuming a uniform extent of both the beam and the source as a first approximation). The resulting column densities are lower limits, since the emitting region could be smaller (Sect. 3.3). We used the affine-invariant MCMC package `emcee` (Foreman-Mackey et al. 2013) with $10^{10} \text{ cm}^{-2} < N_T < 10^{20} \text{ cm}^{-2}$ and $10 \text{ K} < T_{rot} < 500 \text{ K}$ flat priors to estimate the COM column densities and excitation temperatures that best fit (i.e., the 50th percentile from the posteriors) the observed population diagrams according to Eq. C7. Additional information on the MCMC fitting can be found in Loomis et al. (2018) and Bergner et al. (2019).

Table 2 presents the estimated excitation temperatures and column densities for the detected O- and N-bearing COMs toward the continuum peak of Ser-emb 11 W. The observed $\text{CH}_3\text{CH}_2\text{OH}$, CH_3OCH_3 , CH_3COCH_3 , NH_2CHO , $^{13}\text{CH}_3\text{CN}$, and $\text{CH}_3\text{C}^{15}\text{N}$ transitions did not span a wide enough range of upper level energies. In these cases a fixed rotational temperature was adopted in order to estimate their column densities. In particular, the CH_3OH temperature was used for the O-bearing COMs $\text{CH}_3\text{CH}_2\text{OH}$, CH_3OCH_3 , and CH_3COCH_3 , and the average value of $T_{rot}(\text{CH}_2\text{DCN})$ and $T_{rot}(\text{CH}_3\text{CH}_2\text{CN})$ for the N-bearing COMs $^{13}\text{CH}_3\text{CN}$ and $\text{CH}_3\text{C}^{15}\text{N}$. Since NH_2CHO is both O- and N-bearing, we estimated two column densities using the CH_3OH and the complex cyanide excitation temperatures. We note that the partition functions of all species except CH_3OH and CH_3OCH_3 do not take into account higher vibrational states ($\nu_T \geq 1$) that could be populated at $T > 100$ K. The CH_3OCHO and $\text{CH}_3\text{CH}_2\text{CN}$ partition functions (and hence column densities) were corrected by a factor of 1.11 (corresponding to a rotational temperature of 110 K and 99 K, respectively, see Table 2) according to Favre et al. (2014) and Heise et al. (1981). For the rest of species, the vibrational contributions to the partition function were not yet available, but we expect these corrections to be smaller compared to other sources of uncertainty. The values reported in Table 2 were cross-checked with those estimated with the SLIM tool within the MADCUBA

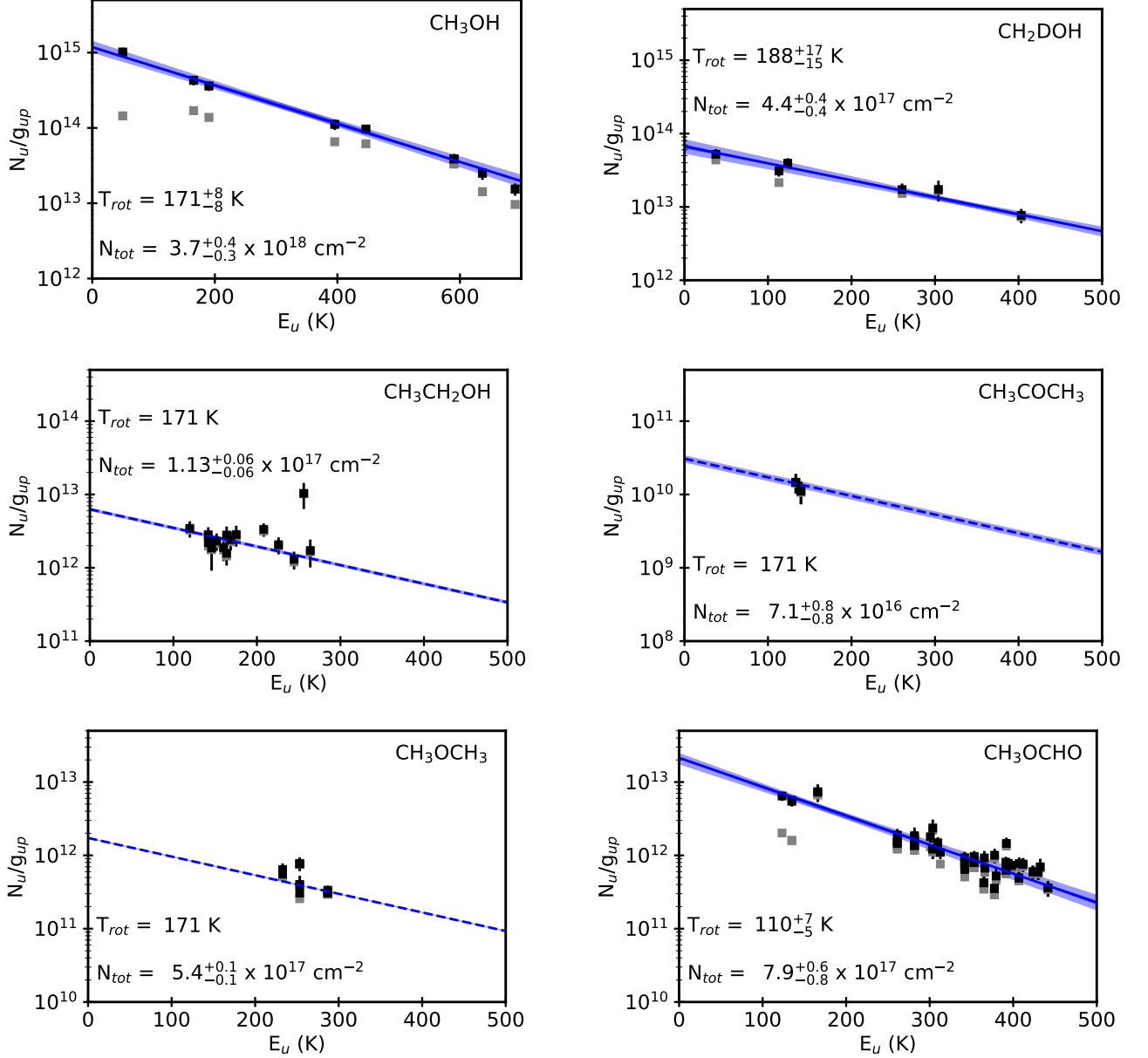


Figure 5. Population diagrams for the detected O-bearing COMs toward Ser-emb 11 W (black squares). The plotted 1σ error bars include a 10% absolute calibration uncertainty, since lines observed with two different frequency settings were used. The upper level populations are corrected according to Eq. C5. The same data points but without the optical depth correction (C_τ) are shown as grey squares to highlight the effects of the line optical depths. The MCMC best-fit to the population diagrams is shown in blue, along with the 1σ confidence region (shaded zone). The estimated best-fit rotational temperature and column density are indicated in every panel. The CH_3OH rotational temperature was adopted in order to estimate the column densities of $\text{CH}_3\text{CH}_2\text{OH}$ and CH_3COCH_3 . In these cases the MCMC best-fit is represented with dashed lines.

package (see Appendix D). The excitation temperatures were within 35%, and the column densities and column density ratios were within a factor of 2.

In all cases where excitation temperatures could be constrained, they were above 100 K, confirming the detection of a hot corino toward Ser-emb 11 W. The O-bearing COMs (except for CH_3OCHO) presented excitation temperatures in the 170–188 K range, higher than

the values estimated for the N-bearing COMs (99–130 K). This pattern is the opposite to that recently observed in the IRAS 16293-2422A hot corino (van’t Hoff et al. 2020). A lower excitation temperature for the N-bearing COMs could indicate that the emission of these species is coming from a colder (or, rather, less warm) region of the inner envelope where COMs are observed. However, neither the emission of O-bearing COMs, nor

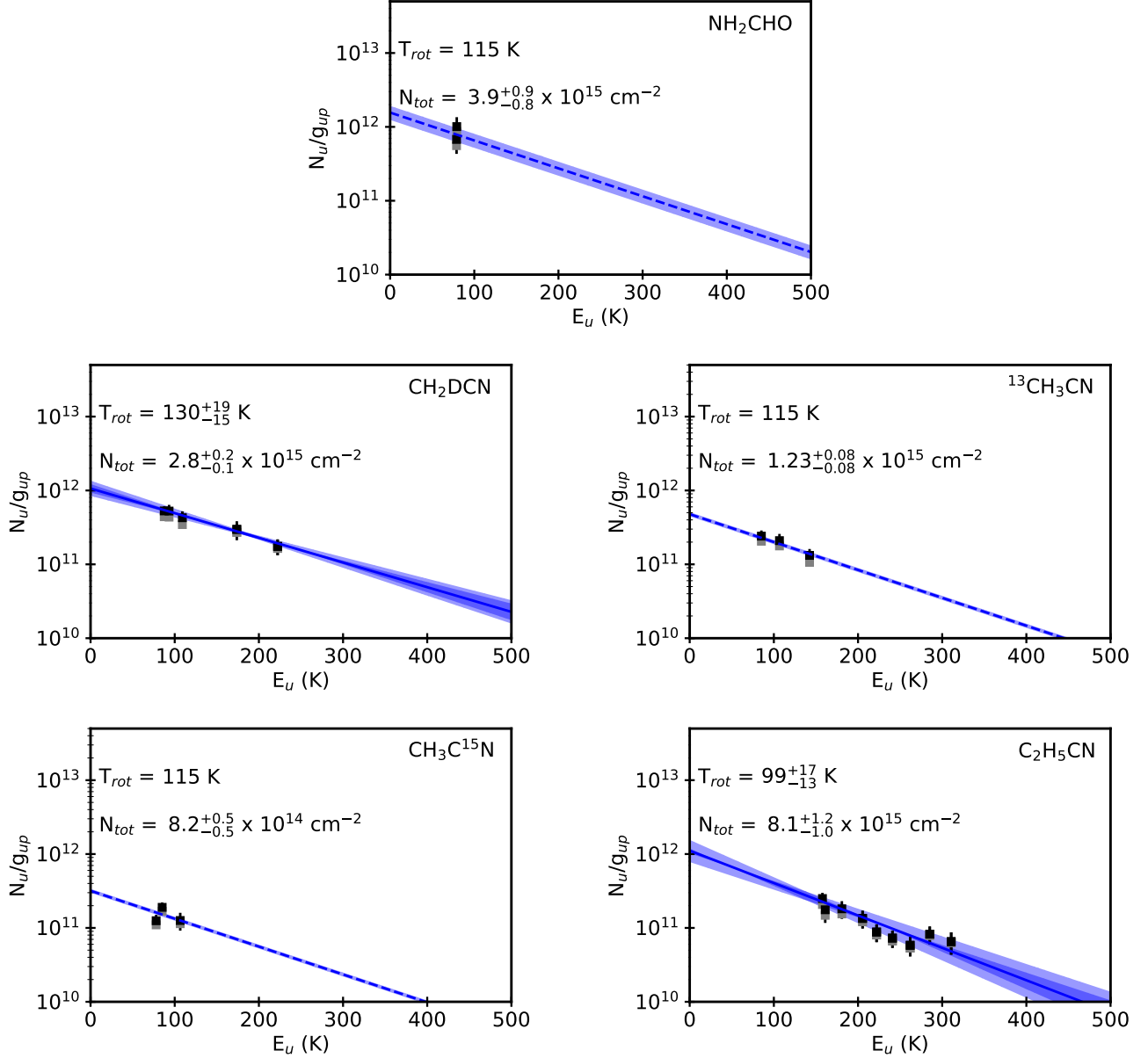


Figure 6. As Fig. 5 but for the detected N-bearing COMs toward Ser-emb 11 W (black squares). The average rotational temperature derived for CH_2DCN and $\text{CH}_3\text{CH}_2\text{CN}$ was adopted in order to estimate the NH_2CHO , $^{13}\text{CH}_3\text{CN}$, and $\text{CH}_3\text{C}^{15}\text{N}$ column densities. In these cases, the MCMC fitting is represented with dashed lines.

N-bearing COMs was resolved within our beam, so a potential different spatial origin of both molecular families could not be evaluated. Higher resolution observations would thus be needed in order to address these differences. The lower excitation temperature found for CH_3OCHO compared to the rest of O-bearing COMs, combined with the narrower FWHM of its emission lines, may indicate that this species is more efficiently destroyed through gas-phase chemical reactions at high temperatures than other O-bearing COMs, and would

be therefore missing in the innermost regions of the hot corino.

The estimated column densities for O-bearing COMs other than CH_3OH range between $7.1 \times 10^{16} \text{ cm}^{-2}$ and $7.8 \times 10^{17} \text{ cm}^{-2}$, while values between $8.2 \times 10^{14} \text{ cm}^{-2}$ and $8.1 \times 10^{15} \text{ cm}^{-2}$ were found for N-bearing COMs. With a CH_3OH column density of $3.7 \times 10^{18} \text{ cm}^{-2}$, this implies column density ratios with respect to CH_3OH of 2–21%, for O-bearing COMs, and 0.02–0.22% for N-bearing COMs.

Table 2. COM column densities and rotational temperatures in the hot corino of Ser-emb 11 W assuming a source size of $\Omega_{source} = 0.17'' \times 0.11''$.

Molecule	T_{rot} (K)	N_T (m^{-2})	$N_T/N_T(\text{CH}_3\text{OH})$ (%)
CH ₃ OH	171 $^{+8}_{-8}$	$(3.7^{+0.4}_{-0.3}) \times 10^{18}$	100
CH ₂ DOH	188 $^{+17}_{-15}$	$(4.4^{+0.4}_{-0.4}) \times 10^{17}$	12
C ₂ H ₅ OH	171 ^a	$(1.13^{+0.06}_{-0.06}) \times 10^{17}$	3.1
CH ₃ OCH ₃	171 ^a	$(5.4^{+0.1}_{-0.1}) \times 10^{17}$	15
CH ₃ OCHO	110 $^{+7}_{-5}$	$(7.8^{+0.6}_{-0.8}) \times 10^{17}$	21
CH ₃ COCH ₃	171 ^a	$(7.1^{+0.8}_{-0.8}) \times 10^{16}$	1.9
NH ₂ CHO	171 ^a	$(5.0^{+1.0}_{-1.0}) \times 10^{15}$	0.14
NH ₂ CHO	115 ^b	$(3.9^{+0.9}_{-0.8}) \times 10^{15}$	0.11
CH ₂ DCN	130 $^{+19}_{-15}$	$(2.8^{+0.2}_{-0.1}) \times 10^{15}$	0.076
¹³ CH ₃ CN	115 ^b	$(1.23^{+0.08}_{-0.08}) \times 10^{15}$	0.032
CH ₃ C ¹⁵ N	115 ^b	$(8.2^{+0.5}_{-0.5}) \times 10^{14}$	0.022
C ₂ H ₅ CN	99 $^{+17}_{-13}$	$(8.1^{+1.2}_{-1.0}) \times 10^{15}$	0.22

NOTE—^aThe C₂H₅OH, CH₃COCH₃, and NH₂CHO column densities were estimated assuming the CH₃OH rotational temperature (Sect. 3.4). ^bThe NH₂CHO, ¹³CH₃CN and CH₃C¹⁵N column densities were estimated assuming the average rotational temperature derived for the complex nitriles.

3.5. Isotopic ratios in Ser-emb 11 W

The reported observations enabled us to estimate three isotopic ratios: CH₂DOH/CH₃OH, CH₂DCN/CH₃CN, and CH₃C¹⁵N/CH₃CN.

The CH₂DOH/CH₃OH abundance ratio is around 12% (Table 2), similar to what has been found in other Class 0/I sources (see, e.g., Bianchi et al. 2019b, and ref. therein), and four orders of magnitude higher than the elemental D/H ratio $\sim 10^{-5}$ (Caselli & Ceccarelli 2012). Previous works have associated high D/H ratios with a solid-state formation pathway at low temperatures (see, e.g., van Gelder et al. 2020).

Assuming a ¹²C/¹³C ratio for the local ISM of 81.3 (Botelho et al. 2020), we estimate a CH₃CN column density of $1.0 \times 10^{17} \text{ cm}^{-2}$ from the ¹³CH₃CN column density listed in Table 2. This would imply a CH₂DCN/CH₃CN abundance ratio of $\sim 3\%$, which is lower than that found for CH₃OH, but similar to what was recently measured toward the Class 0 hot corino IRAS 16293-2422 (Calcutt et al. 2018).

Similarly, the assumed ¹²C/¹³C ratio of 81.3 would imply a CH₃C¹⁵N/CH₃CN column density ratio of $\sim 0.8\%$, corresponding to a ¹⁴N/¹⁵N ratio of ~ 123 . This is ~ 2 times higher than the CH₃C¹⁵N/CH₃CN ratio measured in IRAS 16293-2422 (Calcutt et al. 2018). We note that the CH₃CN column density in that source was derived

from the $\nu_8 = 1$ state, as the main CH₃CN emission lines were optically thick. On the other hand, our ¹⁵N/¹⁴N value in CH₃CN is on the same order as the ¹⁵N/¹⁴N ratio measured for HCN in Class 0/I sources, Class II disks, and comets (Bergner et al. 2020, and references therein).

3.6. Small molecules in Ser-emb 11

Besides the complex organic species listed in Tables 4–8, a number of small O-, N-, and S-bearing molecules (CO, H₂CO, DCN, SO₂, CS, H₂CS, OCS), along with some isotopologues (¹³CO, C¹⁸O, HDCO, H¹³CN, HC¹⁵N, and O¹³CS) were also observed toward the continuum peak of Ser-emb 11 W (and Ser-emb 11 E in some cases), in the two 1.875 GHz wide spectral windows presented in Fig. 3, and dedicated, narrower spectral windows not shown in Fig. 3. The observed transitions corresponding to these smaller species are listed in Table 9 of Appendix B.

Figure 7 presents moment 0 maps of observed emission lines corresponding to the small species listed in Table 9, except for CO, C¹⁸O and H₂CO, shown in Fig. 2. Half of the molecules were detected toward both Ser-emb 11 W and Ser-emb 11 E, although the emission was brighter toward Ser-emb 11 W (except for C¹⁸O and ¹³CO), while the rest were only observed toward Ser-emb 11 W. In particular, CO, ¹³CO and C¹⁸O were

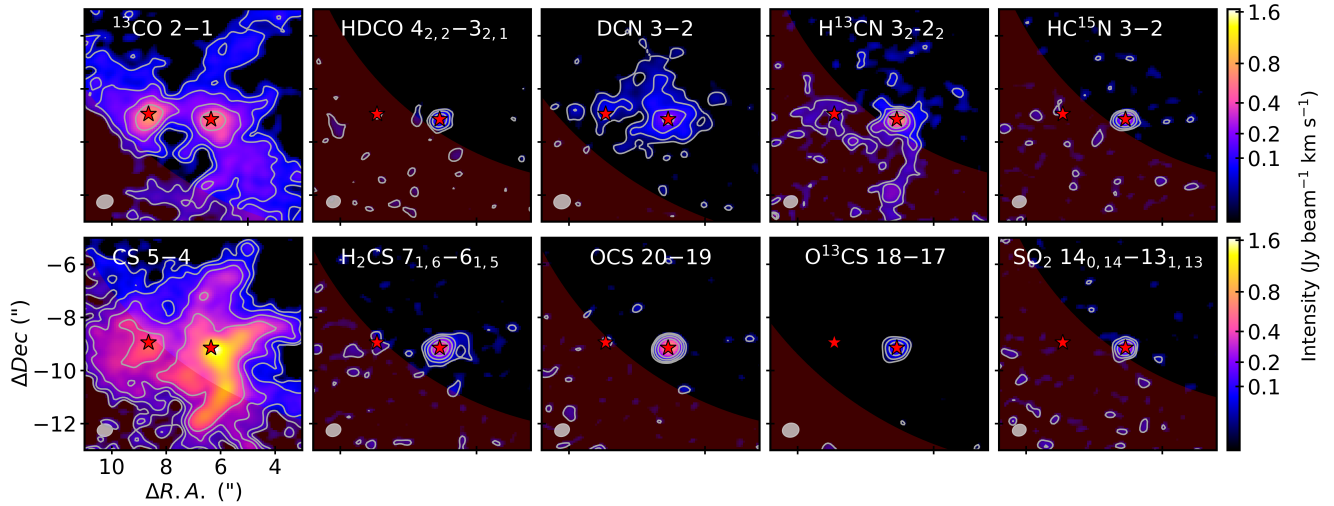


Figure 7. Integrated moment 0 maps toward Ser-emb 11 E and Ser-emb 11 W with the 3, 6, 12, and 24σ contours of the observed emission lines corresponding to the small species listed in Tables 8 and 9 of Appendix B. The position of the continuum emission peak is marked with a star symbol in each panel. Maps are clipped at 2σ . The size of the synthesized beam is shown on the lower left corner of every panel. The region of the field of view observed outside the half power beam width of the primary beam is colored in red.

detected toward both sources. So were the H_2CO ($3_{0,3} - 2_{0,2}$), shown in the fourth panel in Fig. 2, and ($3_{2,2} - 2_{2,1}$) emission lines, that presented a lower intensity toward Ser-emb 11 E, while HDCO was not detected at all toward this component. DCN (and tentatively H^{13}CN) was observed toward both protostars (although with a higher intensity toward Ser-emb 11 W), with the other isotopologue (HC^{15}N) not detected toward Ser-emb 11 E. Among the S-bearing species, only CS was observed toward both sources, but again the emission was fainter toward Ser-emb 11 E.

3.7. Possible rotation signature in Ser-emb 11 W

The C^{18}O $J = 2-1$ emission was selected to study the gas kinematics around both central objects. Fig. 8 shows the high velocity ($\Delta v > 1 \text{ km/s}$) integrated redshifted and blueshifted C^{18}O $J = 2-1$ emission with respect to the systemic velocity of the components (V_{LSR}). For the purpose of this Section, we adopted as the V_{LSR} the velocity position of the C^{18}O $2-1$ intensity peak within a $2''$ region around the continuum peak of each component ($\sim 6.5 \text{ km/s}$ and $\sim 8.2 \text{ km/s}$ for Ser-emb 11 E and Ser-emb 11 W, respectively) We note that both components are part of the same cloud, and the differences in V_{LSR} (as defined above) may be due to a combination of coarse spectral resolution, self-absorption, and/or the presence of infalling material or outflows along the line of sight.

While in Ser-emb 11 E the high-velocity, redshifted C^{18}O emission is located in the same region as the

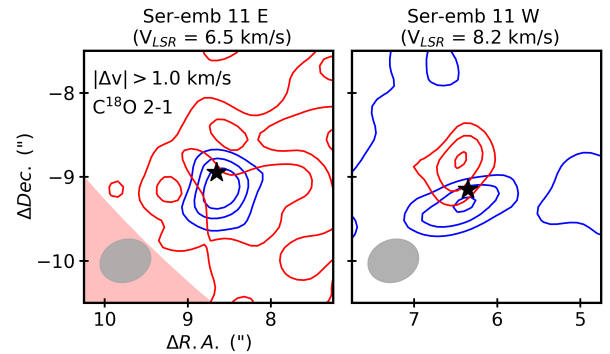


Figure 8. 6, 9, and 12σ contours ($\sigma \sim 4.5 \text{ mJy}$) of the high velocity ($\Delta v > 1 \text{ km/s}$) integrated blue- and red-shifted C^{18}O $2-1$ emission toward Ser-emb 11 E (left panel) and Ser-emb 11 W (right panel). The position of the continuum emission peaks is marked with a star symbol in each panel. The size of the synthesized beam is shown on the lower left corner of each panel. The region of the field of view observed outside the half power beam width of the primary beam is colored in red.

blueshifted emission (left panel of Fig. 8), in Ser-emb 11 W the emission is spatially distributed from redshifted to blueshifted velocities in the N-S direction of a compact region around the central protostar (top right panel of Fig. 8). A velocity gradient across a protostar can originate from outflows, infall, and/or rotation of the molecules around the central object. We note that even when rotation is observed, it does not necessarily imply the presence of a rotationally supported disk, since it could also trace the rotating motion of the infalling

envelope. In the case of Ser-emb 11 W, the presence of a protostellar disk was suggested in Enoch et al. (2011) due to the substantial ~ 230 GHz continuum flux detected at intermediate uv distances (30–100 λ). The velocity gradient observed for the $C^{18}O$ emission in the right panel of Fig. 8 could be due to this putative disk. However, our current observations do not allow us to exclude other possibilities. For example, it could be related to the v-shaped outflow seen in the CO J = 2–1 emission (Fig. 13 in Appendix E). Unfortunately, the ^{12}CO and ^{13}CO emission is too complex to deduce the precise outflow direction. Higher spatial resolution observations are needed to confirm the presence of a protostellar disk in Ser-emb 11 W.

3.8. Organic chemistry toward Ser-emb ALMA 1

Fig. 9 presents an overview of the additional millimeter source detected in Fig. 1, as traced by the millimeter continuum emission, as well as the line emission corresponding to ^{13}CO , $C^{18}O$, CS, SO_2 , DCN, H_2CO , and CH_3OH . The millimeter continuum emission peak is located at $R.A._{J2000} = 18h\ 29m\ 05.61s$, $Dec._{J2000} = +00^\circ\ 30'\ 34.9''$. This source does not have an IR counterpart in any of the four IRAC bands or the 24 μm and 70 μm MIPS bands observed as part of the Spitzer Legacy project "From Molecular Cores to Planet-forming Disks" ("c2d", Evans et al. 2003). Therefore, it was not included in the catalog of 235 Serpens YSOs identified in Harvey et al. (2007), from which 34 sources (Ser-emb 1–34) were further classified as embedded protostars associated with Bolocam 1.1 mm cores in Enoch et al. (2009). We have named this previously not catalogued millimeter source Ser-emb ALMA 1.

Interestingly, no emission coming from any CO isotopologue was detected toward this new millimeter source. Simple N-bearing molecules were not detected either. Among the small molecules detected in Ser-emb 11 and listed in Table 9, only CS (but no other S-bearing species) was detected toward Ser-emb ALMA 1, along with the COM precursor H_2CO . In addition, the CH_3OH ($5_{1,4} - 4_{1,3}$) emission line ($E_{up} = 49.66$ K) was also detected, but no other methanol or COM lines were detected. Therefore, Ser-emb ALMA 1 does probably not host a hot corino, even though it presents CH_3OH emission.

In the case of the CS ($5-4$), H_2CO ($3_{0,3} - 2_{0,2}$), and CH_3OH ($5_{1,4} - 4_{1,3}$) transitions shown in Fig. 9, the emission is resolved around the continuum emission peak, and shows an elongated distribution across the north-west (NW) to south-east (SE) direction with respect to the continuum peak. Fig. 10 shows the inte-

grated emission maps of the detected lines decomposed into the redshifted and blueshifted channels with respect to the systematic velocity of the source ($V_{LSR} = 8.3$ km/s, according to the intensity peak of the H_2CO ($3_{0,3} - 2_{0,2}$) emission detected at the continuum peak of this source). In all cases, the redshifted emission is predominantly detected toward the NW of the continuum peak, while the blueshifted emission is located to the SE. This could indicate the presence of an outflow, infall, and/or rotation of the molecules around the central object.

4. DISCUSSION

The detection of complex organic chemistry (Sect. 3.2) in a compact region around the western component of the Ser-emb 11 binary system (Sect. 3.3), with excitation temperatures above 100 K (Sect. 3.4) indicates that this source hosts a hot corino. If we adopt the classification established in Enoch et al. (2009) (see Sect. 1), Ser-emb 11 W would represent only the fourth hot corino detected toward a Class I source to date.

It is unclear why the number of currently detected Class 0 hot corino sources is much higher than the number of Class I hot corinos. Yang et al. (2021) recently investigated the relation between the protostellar physical properties and the occurrence of COMs in the PEACHES survey sample, and found no clear correlation between the detection of COMs and the bolometric temperature. In addition, they did not find any obvious trend between the number of detected COMs and the bolometric luminosity of the sources either, even though lower luminosities should correspond to a smaller size for the regions where the temperature would be above the ice desorption temperature. The explanation behind the smaller number of hot corinos currently detected toward Class I sources could be instead related to the physical structure (density and temperature profile) of the envelope of the Class I sources on the disk formation scales (Artur de la Villarmois et al. 2019). In a different survey toward a sample of 12 Class I sources in the Ophiuchus star-forming region, no CH_3OH emission toward the continuum peak of any of the sources was detected. However, when a constant density profile corresponding to the flattening of the inner envelope was assumed (as opposed to a centrally-peaked power law density profile typical of Class 0 sources), the resulting upper limits were comparable to the detected abundances toward Class 0 hot corinos (Artur de la Villarmois et al. 2019). In any case, more observations and higher statistics are needed to evaluate whether the occurrence of hot corinos is actually lower toward Class I sources.

4.1. Chemical differentiation in binary sources

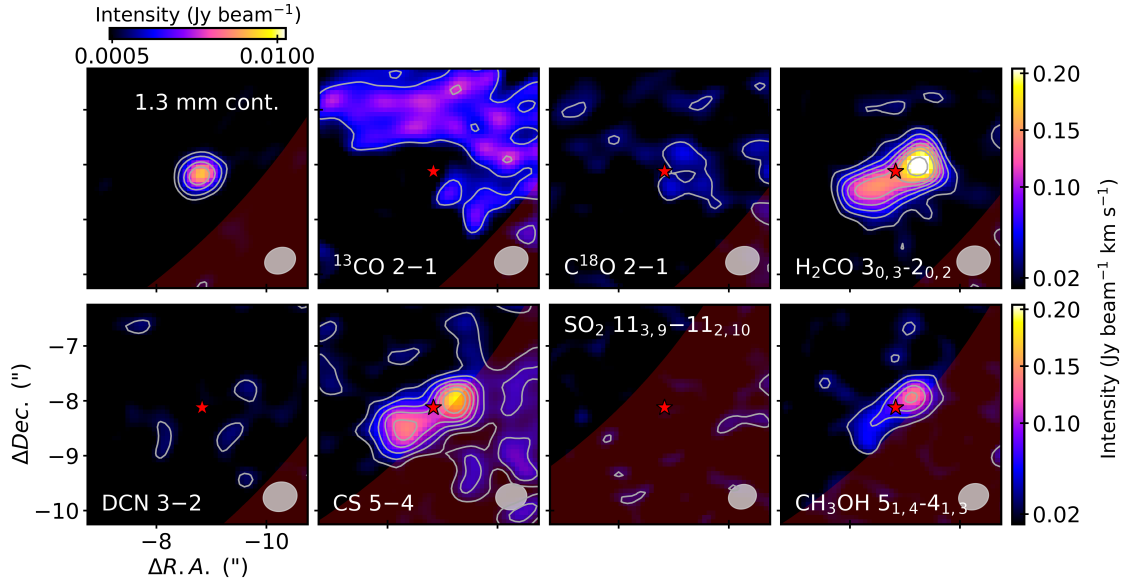


Figure 9. 232 GHz continuum, ^{13}CO , C^{18}O , H_2CO , DCN, CS, SO_2 , and CH_3OH integrated emission maps toward Ser-emb ALMA 1, along with the 3, 6, 12, and 18σ contours in white. The position of the continuum emission peak is marked with a star symbol in each panel. Maps are clipped at 1σ . The size of the synthesized beam is shown on the lower right corner of each panel. The region of the field of view observed outside the half power beam width of the primary beam is colored in red.

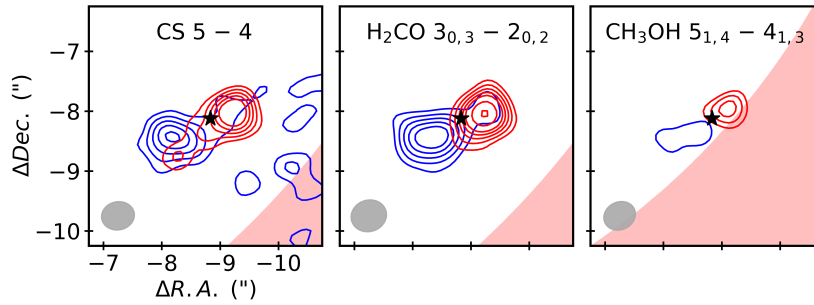


Figure 10. 6, 9, 12, 15, and 18σ contours ($\sigma \sim 6$ mJy) of the integrated blue- and red-shifted CS (5–4), H_2CO ($3_{0,3} - 2_{0,2}$), and CH_3OH ($5_{1,4} - 4_{1,3}$) emission toward the additional millimeter source ($|\Delta v| \sim 0\text{--}2.5$ km/s, V_{LSR} is assumed to be 8.3 km/s, Sect. 3.8). The position of the continuum emission peak is marked with a star symbol in each panel. The synthesized beam is shown on the lower left corner of every panel. The region of the field of view observed outside the half power beam width of the primary beam is colored in red.

In the Ser-emb 11 binary source, hot corino chemistry has been detected only toward the western component, while the eastern component presented no signs of COM emission (Sect. 3.2). Two of the four binary sources with observed hot corino chemistry in Table 1 also presented a similar chemical differentiation, with COMs initially detected in only one of the two components (IRAS 4A2, and SVS13-A VLA4A, see López-Sepulcre et al. 2017; Bianchi et al. 2019a, respectively). In L1551-IRS5, on the other hand, the hot corino emission is brighter toward the N component, but a second hot corino associated with the S component cannot be excluded (Bianchi et al. 2020). Even the binary sources with hot corino chemistry detected toward both com-

ponents present some chemical differences. In IRAS 16293-2422, both the A and B components harbor a hot corino. However, significant differences in the abundance of some COMs relative to CH_3OH between the two components have been reported (Manigand et al. 2020). This apparent chemical differentiation in binary systems has also been found in sources from the CALYPSO (Belloche et al. 2020) and PEACHES (Yang et al. 2021) surveys.

The origin of these differences between binary components is not clear, and could be different for different sources. As mentioned in the introduction, the two components of a chemically differentiated binary system could be at different evolutionary stages or present dif-

ferent physical conditions. In the case of Ser-emb 11, the lower intensity of the continuum emission detected toward Ser-emb 11 E may indicate that the temperature of this source is lower. Assuming that the COMs detected toward Ser-emb 11 W were sublimated from the ice mantles upon passive heating of the inner envelope (see also Sect. 3.3), this could mean that the temperature toward Ser-emb 11 E is not high enough to induce thermal desorption of the ice mantles in the inner regions of its envelope.

Another possibility is that the dust opacity could be different toward the two components of the binary system, hindering the COM detection in one of them. In the case of the IRAS 4A binary source, recent observations of complex organics (CH_3OH , $^{13}\text{CH}_3\text{OH}$, CH_2DOH , and CH_3CHO) seen in absorption at millimeter wavelengths (Sahu et al. 2019), as well as CH_3OH emission observed at centimeter wavelengths (De Simone et al. 2020) suggest that IRAS 4A1 could also harbor a hot corino similar to that observed toward IRAS 4A2, but obscured by the dust continuum opacity. In Section 3.6 we show that the emission of some of the small species observed in Ser-emb 11 is fainter toward Ser-emb 11 E. This could be also due to a higher dust continuum opacity in Ser-emb 11 E that could be blocking the COM millimeter emission. However, the lower intensity of the continuum emission detected toward this component compared to Ser-emb 11 W makes this possibility less likely than in the case of IRAS 4A (although it could just mean that the (maybe optically thick) dust in Ser-emb 11 E is at a lower temperature). Follow-up observations at centimeter wavelengths would be needed to check whether the potential Ser-emb 11 E COM millimeter emission is actually blocked by dust.

4.2. Organic composition in Class 0 and Class I hot corinos

The variation in the chemical composition across different hot corino sources is currently unclear. In the literature, there is evidence supporting both differences in the COM relative abundances of more than one order of magnitude from one hot corino to another (e.g., Bergner et al. 2019; Belloche et al. 2020), and relatively similar COM abundance ratios between different hot corinos (e.g., van Gelder et al. 2020; Yang et al. 2021). One potential issue when comparing reported abundances across different sources is that the COM relative abundances with respect to CH_3OH may be affected by large uncertainties in the estimated CH_3OH column densities, due to line optical depth effects that are treated differently across different works. (see, e.g., the order of magnitude difference in the Ser-emb 8 COM

relative abundances reported in Bergner et al. 2019; van Gelder et al. 2020).

Previous studies focusing on the COM composition of Class I hot corinos compared to Class 0 hot corinos found no substantial differences between the two groups, but the sample of Class I hot corinos was small (SVS13-A, Ser-emb 17, and L1551 IRS5 Bianchi et al. 2019b; Bergner et al. 2019; Bianchi et al. 2020, respectively). According to the classification in Enoch et al. (2009), Ser-emb 11 W would represent the fourth hot corino detected toward a Class I source to date, although its low bolometric temperature (77 K, Enoch et al. 2009) may indicate that this source is rather in a transitional stage between the Class 0 and Class I stages (Sect. 1). In any case, in order to compare the chemical composition across Class 0 and Class I hot corinos, Fig. 11 presents the COM relative abundances with respect to CH_3OH of commonly detected O- and N-bearing COMs, as reported in the literature for the hot corinos in Table 1 (except for IRAS 4B, since only single-dish observations have been reported toward this source, Bottinelli et al. 2007), along with those presented in this work for Ser-emb 11 W. In Fig. 11 (and also Fig. 12), we have considered Ser-emb 11 W as a Class I source, but we note that the subsequent analysis would not be affected if this source was considered instead a transitional Class 0/I source. The reported COM column densities in the different Class 0 and Class I hot corinos are listed in Tables 11 and 12 (respectively) of Appendix F.

The COM relative abundances estimated in this work for the Ser-emb 11 W hot corino (red stars in Fig. 11) are similar to those found toward the three Class I hot corinos previously reported in the literature (red circles in Fig. 11), with typical differences around a factor of a few. A larger scatter (around 1–2 orders of magnitude) is observed for the COM relative abundances in Class 0 hot corinos (blue circles in Fig. 11), as previously suggested in the literature (e.g., Bergner et al. 2019; Belloche et al. 2020).

In order to compare the COM relative abundances in Class I hot corinos with those measured toward Class 0 hot corinos, Fig. 11 also shows the median relative abundances, along with the lower and upper abundance quartiles, found for the O- and N-bearing COMs toward the two groups. The range between the lower and upper abundance quartiles are comparable in Class 0 and Class I hot corinos for CH_2DOH , $\text{C}_2\text{H}_5\text{OH}$, and CH_3CN ; while the rest of studied O- and N-bearing COMs present higher abundances with respect to CH_3OH toward Class I hot corinos. We note that CH_2CO has only been detected in the Ser-emb 17 Class I hot corino, CH_3CHO only in the SVS-13A Class I hot corino, and $^{13}\text{CH}_3\text{CN}$,

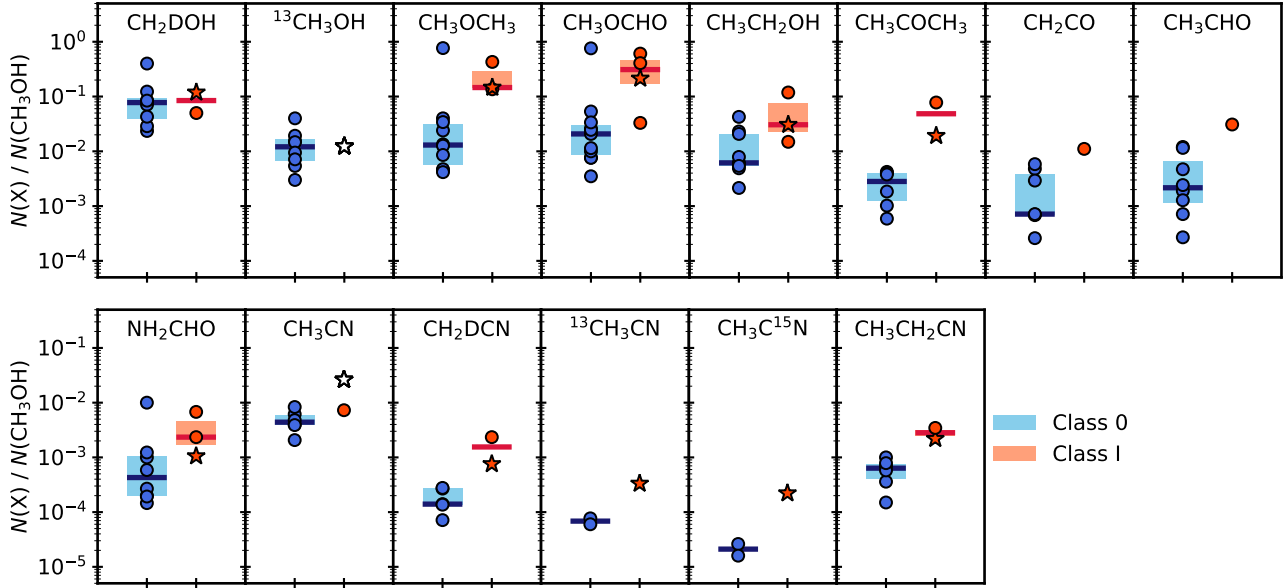


Figure 11. COM relative abundances with respect to CH_3OH for a series of O-bearing (top panels) and N-bearing (bottom panels) species, measured toward Class 0 (blue markers) and Class I (red markers) hot corinos. The values are extracted from the literature (Appendix F), except for the Class I Ser-emb 11 W hot corino, reported in Table 2 (red stars). The $^{13}\text{CH}_3\text{OH}$ abundance in Ser-emb 11 W (white marker) corresponds to a $^{12}\text{C}/^{13}\text{C}$ ratio of 81.3 for the local ISM (Botelho et al. 2020). The CH_3CN abundance in Ser-emb 11 W (white marker) has been estimated from the $^{13}\text{CH}_3\text{CN}$ abundance assuming the above $^{12}\text{C}/^{13}\text{C}$ ratio. For those species with detections in more than one Class 0 and/or Class I hot corino, solid lines indicate the median abundances found in the sample. When the species is detected in more than two Class 0 and/or Class I hot corinos, color bars represent the range between the lower and upper abundance quartiles (i.e., half of the hot corino sources have abundances in that range).

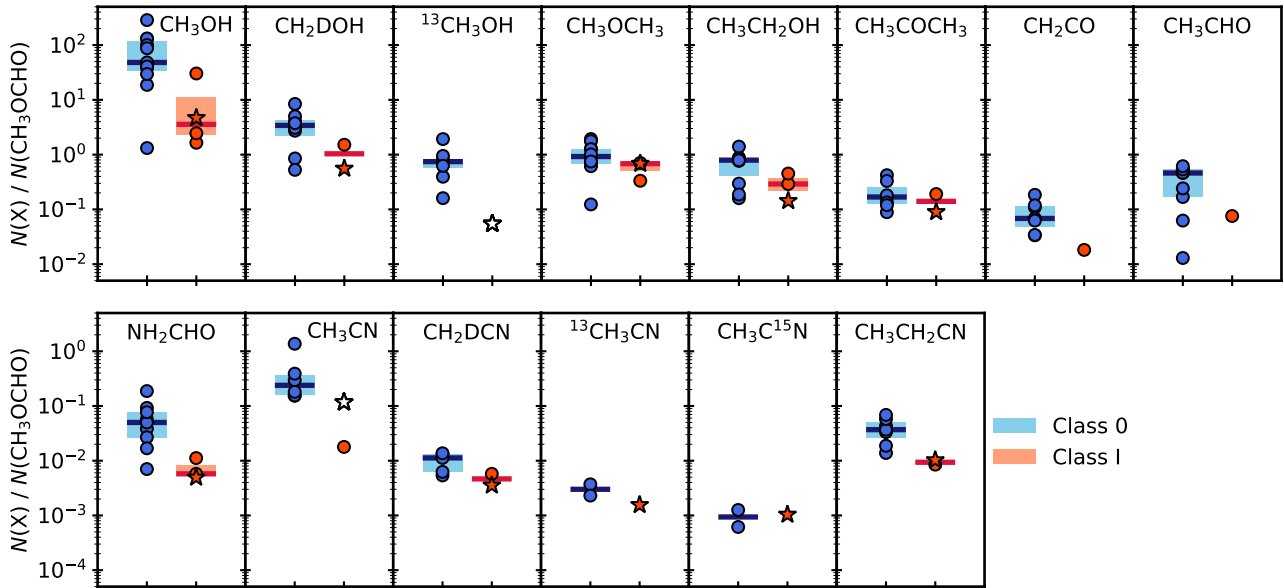


Figure 12. Same as Fig. 11 but with COM relative abundances calculated with respect to CH_3OCHO .

and $\text{CH}_3\text{C}^{15}\text{N}$ only in the Class I (or Class 0/I) Ser-emb 11 hot corino. These putative differences thus need to be confirmed.

Bianchi et al. (2019b, 2020) stated that a more reliable comparison of COM relative abundances across different sources can be obtained using species with reliably optically thin emission as references. Fig. 12 presents the

COM relative abundances with respect to CH_3OCHO (though we note that a few CH_3OCHO emission lines were optically thick toward our source). In this case, the ranges between the lower and upper abundance quartiles of all COMs other than CH_3OH are within a factor of a few in Class 0 and Class I hot corinos, except for NH_2CHO and CH_3CN . Nazari et al. (2021) have recently reported a large scatter in the NH_2CHO abundances measured across various sources (including low- and high-mass YSOs). These differences were attributed to the multiple formation pathways proposed in the literature for this species, whose abundance could depend on the local source conditions to a larger extent compared to other COMs. We also note that CH_3CN has only been detected toward only one Class I hot corino, and the abundance in Ser-emb 11 W estimated from the observed $^{13}\text{CH}_3\text{CN}$ column density is consistent with that measured toward Class 0 hot corinos. Recent works have shown that a tight correlation in the N-bearing COM relative abundances across different sources is found when another N-bearing species such as HNCO or CH_3CN is used as reference (Jørgensen et al. 2020; Nazari et al. 2021). However, we have not carried out such comparison in this work, since neither HNCO nor CH_3CN column densities have been measured toward Ser-emb 11 W, and they have not been reported either for more than half of the sources in our sample.

Based on these comparisons, we do not find any evidence of a significant evolution in the complex organic chemistry between Class 0 and Class I hot corinos. This suggests that the complex organic composition around low-mass protostars is likely shaped by the ice chemistry that takes place in the parental molecular cloud and the chemical pathways that are activated during the warm-up of the ice mantles prior to their desorption (Öberg & Bergin 2020).

5. CONCLUSIONS

1. Five O-bearing COMs (CH_3OH , $\text{CH}_3\text{CH}_2\text{OH}$, CH_3OCH_3 , CH_3OCHO , and CH_3COCH_3) and three N-bearing COMs (NH_2CHO , CH_2DCN , and $\text{CH}_3\text{CH}_2\text{CN}$), as well as three isotopologues (CH_2DOH , $^{13}\text{CH}_3\text{CN}$, and $\text{CH}_3\text{C}^{15}\text{N}$) have been detected toward the W component of the Ser-emb 11 binary YSO, a Class I source near the Class 0/I cutoff.
2. No complex organic emission was observed toward the Ser-emb 11 E component. This chemical differentiation observed in the Ser-emb 11 binary system is in line with similar observations toward other binary sources. We speculate that the COM emission toward Ser-emb 11 E could be blocked by optically thick dust, as recently observed in the IRAS 4A binary source.
3. The emission of the complex organic species was unresolved in our observations, implying a compact emission region around the central protostar in Ser-emb 11 W ($0.17'' \times 0.11''$ size according to the deconvolved CH_3OH emission). In addition, a population diagram analysis of five of the observed COMs revealed excitation temperatures above 100 K, i.e., the desorption temperature of water ice. This implies the presence of a hot corino in Ser-emb 11 W.
4. The COM relative abundances with respect to CH_3OH in the Ser-emb 11 W Class I hot corino are consistent with those found toward the other three Class I hot corinos previously reported in the literature.
5. The estimated COM relative abundances are similar in the sample of observed Class 0 and Class I hot corinos when they are calculated with respect to a species with optically thin emission lines such as CH_3OCHO . This suggests some level of continuity in the underlying chemistry during the star-formation process.
6. The measured $\text{CH}_2\text{DOH}/\text{CH}_3\text{OH}$ column density ratio was $\sim 11\%$, four orders of magnitude higher than the elemental D/H ratio. Assuming a $^{12}\text{C}/^{13}\text{C}$ ratio of 81.3, we also estimated $\text{CH}_2\text{DCN}/\text{CH}_3\text{CN}$ and $\text{CH}_3\text{C}^{15}\text{N}/\text{CH}_3\text{CN}$ column density ratios of $\sim 3\%$ and $\sim 0.8\%$, respectively (corresponding to a $^{14}\text{N}/^{15}\text{N}$ of ~ 123).
7. The high-velocity $\text{C}^{18}\text{O } J = 2-1$ emission was spatially distributed from redshifted to blueshifted velocities in the N-S direction of a compact region around the central protostar in Ser-emb 11 W. This is compatible with the presence of a protostellar disk in this source, as previously proposed in the literature. However, our current observations do not allow us to exclude other possibilities.
8. Complex organic chemistry (in particular, H_2CO and CH_3OH emission) was also detected toward Ser-emb ALMA 1, a nearby millimeter source that had not been previously catalogued.

ACKNOWLEDGMENTS

This paper makes use of the following ALMA data: ADS/JAO.ALMA#2015.1.00964.S. ALMA is a partnership of ESO (representing its member states), NSF (USA) and NINS (Japan), together with NRC (Canada), MOST and ASIAA (Taiwan), and KASI (Republic of Korea), in cooperation with the Republic of Chile. The Joint ALMA Observatory is operated by ESO, AUI/NRAO and NAOJ. This work was supported by an award from the Simons Foundation (SCOL # 321183, KO). J.B.B. acknowledges funding from the National Science Foundation Graduate Research Fellowship under Grant DGE1144152. C.J.L. acknowledges funding from the National Science Foundation Graduate Research Fellowship under Grant DGE1745303. The group of JKJ is supported by the European Research Council (ERC) under the European Union’s Horizon 2020 research and innovation programme through ERC Consolidator Grant ”S4F” (grant agreement No 646908). Research at Centre for Star and Planet Formation is funded by the Danish National Research Foundation.

Facility: ALMA

Software: CASA (v4.5.3, v4.7.0, 5.4.1, & v5.4.2; (McMullin et al. 2007), MADCUBA (Rivilla et al. 2016, 2017), NumPy (van der Walt et al. 2011), SciPy (Virtanen et al. 2020)

REFERENCES

- ALMA Partnership 2015, ApJL, 808, 1, L3
- Altwegg, K., Balsiger, H., Bar-Nun, A., et al. 2016, Sci. Adv., 2, 5, e1600285
- Andréé, P., Ward-Thompson, D., & Barsony, M. 1993, ApJ, 406, 122
- Andréé, P., Ward-Thompson, D., & Barsony, M. 2000, Protostars and Planets IV, eds. V. Mannings, A.P. Boss, & S.S. Russel (Tucson: Univ. of Arizona Press)
- Arce, H. G., Santiago-García, J., Jørgensen, J. K., Tafalla, M., & Bachiller, R. 2008, ApJ, 681, L21
- Artur de la Villarmois, E., Jørgensen, J.K., Kristensen, L.E., et al. 2019, A&A, 626, A71
- Ball, J.A., Gottlieb, C.A., Lilley, A.E., & Radford, H.E. 1970, ApJL, 162, L203
- Belloche, A., Maury, A.J., Maret, S., et al. 2020, A&A, 635, A198
- Bergner, J.B., Martín-Doménech, R., Öberg, K.I., et al. 2019, ACS Earth and Space Chemistry, 3, 8, 1564
- Bergner, J.B., Öberg, K.I., Bergin, E.A., et al. 2020, 898, 2, id.97
- Bianchi, E., Ceccarelli, C., Codella, C., et al. 2019, ACS Earth and Space Chemistry, 3, 12, 2659
- Bianchi, E., Chandler, C.J., Ceccarelli, C., et al. 2020, MNRAS, 498, 1, L87
- Bianchi, E., Codella, C., Ceccarelli, C., et al. 2019, MNRAS, 483, 2, 1850
- Blake, G.A., Sutton, E.C., Masson, C.R., & Philipps, T.G. 1987, ApJ, 315, 621
- Botelho, R.B., Milone, A. de C., Meléndez, J., et al. 2020, MNRAS, 499, 2, 2196
- Bottinelli, S., Ceccarelli, C., Lefloch, B., et al. 2004, ApJ, 615, 354
- Bottinelli, S., Ceccarelli, C., Williams, J. P., & Lefloch, B. 2007, A&A, 463, 601
- Calcutt, H., Jørgensen, J.K., Müller, H.S.P., et al. 2018, A&A 616, A90
- Caselli, P. & Ceccarellu, C. 2012, A&A Rev., 20, 56
- Cazaux, S., Tielens, A. G. G. M., Ceccarelli, C., et al. 2003, ApJ, 593, L51
- Chandler, C.J., & Richer, J.S. 2000, Astrophys. J., 530, 851
- Charnley, S.B., Tielens, A.G.G.M., & Millar, T.J. 1992, ApJ, 339, L71
- Codella, C., Ceccarelli, C., Cabrit, S., et al. 2016, A&A, 586, L3
- De Simone, M., Ceccarelli, C., Codella, C., et al. 2020, ApJL, 896, L3
- Enoch, M. L., Corder, S., Duchêne, G., et al. 2011, ApJS, 195, 21

- Enoch, M. L., Evans, N. J., II, Sargent, A. I., & Glenn, J. 2009, *ApJ*, 692, 973
- Evans, N.J. II, Allen, L.E., Blake, G.A., et al. 2003, *PASP*, 115, 810, 965
- Favre, C., Carvajal, M., Field, D., et al. 2014, *ApJSS*, 215, 2, id25
- Foreman-Mackey, D., Hong, D.W., Lang, D., & Goodman, J. 2013, *PASP*, 125, 306
- Goldsmith, P.F., & Langer, W.D. 1999, *ApJ*, 517, 209
- Green, J.D., Evans II, N.J., Jørgensen, J.K., et al. 2013, *ApJ*, 770, 123
- Harsono, D., Bjerkele, P., van der Wiel, M.H.D., et al. 2018, *Nature Astronomy*, 2, 646
- Harvey, P., Merín, B., Huard, T.L., et al. 2007, *ApJ*, 663, 1149
- Heise, H.M., Winther, F., & Lutz, H. 1981, *J. Mol. Spectrosc.*, 90, 531
- Herbst, E., & van Dishoeck, E.F. 2009, *ARA&A*, 47, 42
- Hsu, S.-Y., Liu, S.-Y., Lie, T., et al. 2020, 898, 2, id.107
- Imai, M., Sakai, N., Oya, Y., et al. 2016, *ApJ*, 830, L37
- Jacobsen, S.K., Jørgensen, J.K., Di Francesco, J., et al. 2019, *A&A*, 629, A29
- Jørgensen, J.K., Belloche, A., & Garrod, R.T. 2020, *ARA&A*, 58, 727
- Jørgensen, J.K., Bourke, T.L., Myers, P.C., et al. 2005, *ApJ*, 632, 973
- Jørgensen, J.K., Bourke, T.L., Nguyen Luong, Q., & Takakuwa, S. 2011, *A&A*, 534, A100
- Jørgensen, J.K., Müller, H.S.P., Calcutt, H., et al. 2018, *A&A*, 620, A170
- Kahane, C., Jaber Al-Edhari, A., Ceccarelli, C., et al. 2018, *ApJ*, 852, 130
- Lee, C-F., Codella, C., Li, Z.-Y., & Liu, S.-Y. 2019, *ApJ*, 876, 1, id.63
- Lefloch, B., Bachiller, R., Ceccarelli, C., et al. 2018, *MNRAS*, 477, 4792
- Loomis, R., Cleeves, L.I., Öberg, K.I., et al. 2018, *ApJ*, 859, 131
- López-Sepulcre, A., Sakai, N., Neri, R., et al. 2017, *A&A*, 606, A121
- Lykke, J.M., Coutens, A., Jørgensen, J.K., et al. 2017, *A&A*, 597, A93
- Manigand, S., Jørgensen, J.K., Calcutt, H., et al. 2020, *A&A*, 635, A48
- Martín, S., Martín-Pintado, J., Blanco-Sánchez, C., et al. 2019, *A&A*, 631, A159
- Martín-Doménech, R., Bergner, J.B., Öberg, K.I., & Jørgensen, J.K. 2019, *ApJ*, 880, 2, id.130
- McMullin, J.P., Waters, B., Schiebel, D., Young, W., & Golap, K. 2007, *ASPC*, 376, 127
- Milam, S.N., Savage, C., Brewster, M.A., Ziurys, L.M., & Wyckoff, S. 2005, *ApJ*, 634, 1126
- Müller, H. S. P., Schlöder, F., Stutzki, J., & Winnewisser, G. 2005, *JMoSt* 742, 215
- Nazari, P., van Gelder, M.L., van Dishoeck, E.F., et al. 2021, *A&A*, *accepted*
- Öberg, K.I & Bergin, E.A. 2020, *Physics Report*, 893, 1
- Öberg, K. I., Bottinelli, S., Jørgensen, J. K., & van Dishoeck, E. F. 2010, *ApJ*, 716, 1, 825
- Ortiz-León, G.N., Loinard, L., Dzib, S.A., et al. 2018, *ApJ*, 869, 2, L33
- Oya, Y., Sakai, N., López-Sepulcre, A., et al. 2016, *ApJ*, 824, 88
- Oya, Y., Sakai, N., Watanabe, Y., et al. 2017, *ApJ*, 837, 174
- Pezzuto S., Elia, D., Schisano, E., et al. 2012, *A&A*, 547, A54
- Pickett, H. M., Poynter, R. L., Cohen, E. A., et al. 1998, *JQSRT*, 60, 883
- Rivilla, V.M., Fontani, F., Beltrán, M.T., et al. 2016, *ApJ*, 826, 2
- Rivilla, V. M. and Beltrán, M. T., Cesaroni, R., et al. 2017, *A&A*, 598, A59
- Rubin, R.H., Swenson, G.W.J., Benson, R.C., Tigeraar, H.L., & Flygare, W.H. 1971, *ApJL*, 169, L39
- Sahu, D., Liu, S.-Y., Su, Y.N., et al. 2019, *ApJ*, 872, 2, id.196
- Segura-Cox, D.M., Schmiedeke, A., Pineda, J.E., et al 2020, *Nature*, 586, 7828, 228
- Sheehan, P.D., & Eisner, J.A. 2018, *ApJ*, 857, 1, id.18
- Solomon, P.M., Jefferts, K.B., Penzias, A.A., & Wilson, R.W. 1971, *ApJL*, 168, L107
- Taquet, V., López-Sepulcre, A., Ceccarelli, C., et al. 2015, *ApJ*, 804, 81
- Tobin, J.J., Looney, L.W., Li, Z.-Y., et al. 2016, *ApJ*, 818, 1, id.73
- Turner, B.E. 1991, *ApJS*, 76, 617
- Tychoniec, L., Manara, C.F., Rosotti, G.P., et al. 2020, *A&A*, 640, A19
- Tychoniec, L., van Dishoeck, E.F., van't Hoff, M.L.R., et al. 2021, *A&A*, *in press*
- van der Walt, S., Colbert, S.C., Varoquaux, G. 2011, *CiSE*, 13, 2, 22
- van Gelder, M.L.m Tabone, B., Tychoniec, L., et al. 2020, *A&A* 639, A87
- van't Hoff, M.L.R., van Dishoeck, E.F., Jørgensen, J.K., & Calcutt, H. 2020, *A&A* 633, A7
- Virtanen, P., Gommers, R., Oliphant, T.E., et al. 2020, *Nat. Meth.*, 17, 261
- Wilson, T.L. & Rood, R. 1994, *ARA&A*, 32, 191

Yang, Y.-L., Evans, N.J., Smith, A., et al. 2020, *ApJ*, 891, 1, id.61

Yang, Y.-L., Sakai, N., Zhang, Y., et al. 2021, *ApJ*, *accepted*

Table 3. Observed spectral windows

Frequency range (GHz)	Spectral resolution (km s ⁻¹)	Beam size " × "
217.209 – 217.268	0.195	0.62 × 0.53
218.193 – 218.251	0.194	0.62 × 0.53
218.446 – 218.505	0.194	0.60 × 0.52
218.703 – 218.762	0.193	0.60 × 0.52
219.502 – 219.619	0.193	0.62 × 0.50
220.340 – 220.457	0.192	0.62 × 0.50
230.479 – 230.597	0.183	0.59 × 0.47
231.262 – 231.380	0.183	0.58 × 0.47
231.481 – 233.356	1.250	0.58 × 0.47
242.978 – 244.853	1.191	0.56 × 0.47
244.164 – 244.281	0.173	0.57 × 0.47
244.877 – 244.994	0.173	0.57 × 0.47
258.098 – 258.216	0.164	0.53 × 0.44
258.953 – 259.070	0.163	0.52 × 0.45
260.459 – 260.577	0.162	0.52 × 0.44
262.150 – 262.267	0.161	0.52 × 0.44

APPENDIX

A. OBSERVED SPECTRAL WINDOWS

Table 3 lists the spectral windows observed with the two Band 6 frequency settings described in Sect. 2.

B. IDENTIFIED MOLECULAR TRANSITIONS TOWARD SER-EMB 11 W

Tables 4–8 list the identified COM transitions in Fig. 3. In particular, Tables 4–7 present the O-bearing COM detected transitions, while Table 8 lists those corresponding to N-bearing COMs. In addition, Table 9 presents all the transitions corresponding to small (4 atoms or less) O-, N-, and S-bearing molecules observed in Fig. 3 and in dedicated, narrow spectral windows not shown in Fig. 3. The line parameters were extracted from the JPL catalog for CH₃OH, CH₂DOH, and CH₃OCHO, and from the CDMS catalog for CH₃CH₂OH, CH₃OCH₃, CH₃COCH₃, and the five N-bearing COMs. Tentatively detected lines (observed with SNR < 3) corresponding to confirmed species are marked with a * in Tables 4–8, and they were not considered in the discussion. Species with only one line observed at SNR > 3 were considered tentative detections, and are also marked with a *.

As explained in Sect. 3.4, the spectral features observed in Fig. 3 were fitted with a Gaussian using the Levenberg-Marquardt minimization implementation of `scipy.optimize.curve_fit` in Python (except those observed with a SNR < 3). The position, width, integrated intensities, and uncertainties estimated from the Gaussian fits of the lines are also presented.

Transitions marked with an ^a in Tables 4–8 appeared partially blended in Fig. 3 with a transition from a different detected species. As the partially blended emission lines were resolved, different Line IDs were assigned to every transition marked with an ^a. A multiple Gaussian fitting was performed in these cases in order to get the position, linewidth, and integrated intensities of the individual components. For some blended emission lines, as well as isolated, weak lines with SNR close to 3, the linewidth of the different components was fixed as the average linewidth of the two strongest, resolved transitions of the corresponding species. This ensured that emission from neighboring lines and/or noise was not taken into account for the Gaussian fit of every component. In those particular cases, the adopted FWHM is indicated with no uncertainties in Tables 4–8.

In other cases two or more transitions from different species appeared completely blended, and only one emission line was observed in Fig. 3. These transitions are indicated with a ^b in Tables 4–8, and were assigned the same Line ID. The multiple Gaussian fitting was not performed for these lines, as the contribution from the different components could not be disentangled.

When the completely blended transitions corresponded to the same species, a single Gaussian fit was performed in the cases where the blended transitions had the same upper level energy (E_{up}) and Einstein coefficient (A_{ul}). The integrated intensities of the different components were calculated from the total integrated intensity according to their upper level degeneracies (g_{up}).

Finally, the identified transitions marked with a ^c were partially blended with other unidentified transitions. In most cases, a multiple Gaussian fitting allowed the estimation of the position, linewidth and integrated intensity of the identified transition. A fixed linewidth was adopted when necessary, as explained above.

We note that the uncertainties in the position and FWHM of the lines only take into account the fitting errors. The real uncertainties are expected to be larger due to the spectral resolution of the observations (Table 3).

C. POPULATION DIAGRAM ANALYSIS

According to Goldsmith & Langer (1999), if local thermodynamical equilibrium (LTE) is assumed in the observed region, the integrated intensity ($\int S_\nu dv$) of a transition is directly proportional to the population of the corresponding upper level (N_u), provided that the emission line is optically thin:

$$\int S_\nu dv = A_{ul}hc \times N_u \times \frac{\Omega}{4\pi}, \quad (\text{C1})$$

where A_{ul} is the Einstein coefficient of the transition (indicated in Tables 4 – 9 for every detected transition in our observations), h is the Planck constant, c the speed of light, and Ω is the solid angle subtended by the emitting region.

The population of the upper level can thus be calculated for a particular transition from the observed integrated intensity according to Eq. C2:

$$N_{u,obs} = \frac{4\pi \int S_{\nu,obs} dv}{A_{ul}\Omega hc}. \quad (\text{C2})$$

The synthesized beam solid angle of the observations is used as Ω when deriving beam-averaged column densities. If the emitting region is smaller than the beam size (i.e., the emission is not spatially resolved), the observed integrated flux density would be assumed to be emitted from a region larger than the actual emitting region, and the resulting beam-averaged column density would be underestimated compared to the actual column density in the source. This so-called beam dilution effect can be corrected by applying the filling factor $\Omega_{beam}/\Omega_{source}$ to Eq. C2 (assuming that both the beam and source extent are uniform).

A correction factor C_τ should also be applied to the observed integrated intensities in Eq. C2 to account for the optical depths of the emission lines (see also Taquet et al. 2015; Loomis et al. 2018; Bergner et al. 2019):

$$C_\tau = \frac{\tau}{1 - e^{-\tau}} \quad (\text{C3})$$

where τ is the optical depth of any emission line, determined by:

$$\tau = \frac{c^3 A_{ul} N_u}{8\pi\nu^3 \Delta\nu} (e^{h\nu/kT_{rot}} - 1), \quad (\text{C4})$$

where ν is the line frequency, $\Delta\nu$ is the line FWHM (also indicated in Tables 4 – 9), k is the Boltzmann constant, and T_{rot} is the rotational temperature of the species.

Altogether, the corrected upper level population can be calculated as:

$$N_u = N_{u,obs} C_\tau \frac{\Omega_{beam}}{\Omega_{source}} \quad (\text{C5})$$

At the same time, the upper level population N_u corresponding to any transition is related to the total column density N_T of the species and its excitation temperature T_{rot} according to the Boltzmann equation:

$$N_u = N_T \frac{1}{e^{E_{up}/T_{rot}}} \frac{g_{up}}{Q(T_{rot})}, \quad (\text{C6})$$

where g_{up} and E_{up} are the upper level degeneracy and upper level energy of the transition, respectively, in K (also indicated in Tables 4 – 9 for the detected transitions), and $Q(T_{rot})$ is the partition function of the species. The partition function of every species was extracted from the same catalog as the rest of line parameters, except for CH_3COCH_3 , for which the partition function was extracted from the JPL catalog, since it was not available in the CDMS catalog.

When several transitions spanning a wide range of upper level energies are observed for a particular species, the relation between the measured N_u/g_{up} ratio and E_{up} of every transition can be described with an exponential function:

$$\frac{N_u}{g_{up}} = \frac{N_T}{Q(T_{rot})} e^{-E_{up}/T_{rot}}. \quad (\text{C7})$$

Since N_u depends on the rotational temperature through the optical depth correction factor C_τ (Eq. C5),

Table 4. Identified O-bearing COM transitions toward the continuum peak of Ser-emb 11 W. The list includes 3 species and 1 isotopologue (CH₃OCH₃ and CH₃OCHO detected transitions are presented in Tables 5–7). Tentative detections are indicated with a *. Integrated intensity maps of boldfaced transitions are presented in Fig. 4.

Line ID	Molecule	Transition	Frequency (GHz)	$\log_{10}(A_{ul})$ (s ⁻¹)	g_{up}	E_{up} (K)	V_{LSR} (km s ⁻¹)	FWHM	Integrated Intensity (mJy beam ⁻¹ km s ⁻¹)
1	t-HCOOH*	10 _{1,9} – 9 _{1,8}	231.506	-3.88	21	64.47	9.87 ± 0.42	4.00 ± 0.76	80.1 ± 18.0
123	CH ₂ CO*	12 _{1,11} – 11 _{1,10}	244.714	-3.79	75	89.42	11.11 ± 0.20	3.47 ± 0.49	80.4 ± 14.7
35	CH ₃ OH ^a	10 _{2,8} – 9 _{3,7} A	232.418	-4.73	21	165.40	8.18 ± 0.06	4.46 ± 0.16	522.1 ± 22.6
44	CH ₃ OH	18 _{3,16} – 17 _{4,13} A	232.783	-4.66	37	446.53	8.18 ± 0.05	4.14 ± 0.13	393.2 ± 16.2
50	CH₃OH	10_{3,7} – 11_{2,9} E	232.946	-4.67	21	190.37	9.00 ± 0.05	4.22 ± 0.13	487.7 ± 19.4
89	CH ₃ OH	18 _{6,13} – 19 _{5,14} A	243.397	-4.70	37	590.28	8.43 ± 0.07	4.52 ± 0.19	(386.6 ± 21.3)/2
89	CH ₃ OH	18 _{6,12} – 19 _{5,15} A	243.398	-4.70	37	590.28	8.43 ± 0.07	4.52 ± 0.19	(386.6 ± 21.3)/2
90	CH ₃ OH	23 _{3,20} – 23 _{2,21} A	243.413	-4.11	47	690.08	9.31 ± 0.10	3.88 ± 0.25	276.3 ± 23.1
97	CH ₃ OH	5 _{1,4} – 4 _{1,3} A	243.916	-4.22	11	49.66	9.00 ± 0.04	4.36 ± 0.14	754.8 ± 30.1
111	CH ₃ OH ^a	22 _{3,19} – 22 _{2,20} A	244.330	-4.11	45	636.75	8.02 ± 0.12	4.13 ± 0.30	391.4 ± 32.7
112	CH ₃ OH $\nu=1$	9 _{-1,9} – 8 _{-0,8} E	244.338	-4.39	19	395.64	8.76 ± 0.07	4.01 ± 0.18	399.5 ± 22.8
10	CH ₂ DOH ^a	10 _{1,9} – 9 _{2,8} e ₀	231.840	-4.78	21	123.70	7.88 ± 0.13	3.54	99.1 ± 7.0
19	CH₂DOH	9_{2,7} – 9_{1,8} e₀	231.969	-4.06	19	113.11	9.08 ± 0.08	4.08 ± 0.20	279.5 ± 17.6
60	CH ₂ DOH	14 _{2,12} – 14 _{1,13} o ₁	233.142	-4.52	29	260.58	9.47 ± 0.10	3.03 ± 0.26	105.0 ± 11.7
66	CH ₂ DOH ^{a,c}	17 _{2,15} – 17 _{1,16} e ₀	233.210	-4.05	35	347.06
85	CH ₂ DOH ^b	5 _{2,3} – 5 _{1,4} e ₀	243.226	-4.18	11	48.40
98	CH ₂ DOH	16 _{1,16} – 15 _{2,14} e ₁	243.960	-4.96	33	304.06	8.17 ± 0.19	2.75 ± 0.46	47.3 ± 10.3
114	CH ₂ DOH ^b	11 _{2,10} – 11 _{1,11} e ₁	244.490	-4.89	23	167.89
120	CH ₂ DOH ^b	7 _{1,6} – 6 _{2,4} o ₁	244.588	-4.73	15	83.33
125	CH ₂ DOH ^c	18 _{3,16} – 17 _{4,13} e ₀	244.825	-4.59	37	403.20	8.02 ± 0.28	3.54	54.7 ± 6.7
126	CH ₂ DOH ^a	4 _{2,2} – 4 _{1,3} e ₀	244.841	-4.32	9	37.59	8.59 ± 0.07	3.00 ± 0.17	147.9 ± 11.1
2	t-CH₃CH₂OH	21_{5,17} – 21_{4,18}	231.559	-4.08	43	225.89	9.98 ± 0.35	3.55	55.3 ± 8.9
2	t-CH₃CH₂OH^c	21_{5,16} – 21_{4,17}	231.561	-4.08	41	208.15	8.70 ± 0.24	3.55	85.2 ± 9.1
3	g-CH ₃ CH ₂ OH	14 _{1,14} – 13 _{1,13}	231.669	-3.96	29	141.86	9.01 ± 0.15	2.46 ± 0.37	49.8 ± 9.9
5	t-CH ₃ CH ₂ OH ^b	19 _{5,15} – 19 _{4,16}	231.738	-4.13	39	191.32
7	t-CH ₃ CH ₂ OH	22 _{5,18} – 22 _{4,19}	231.790	-4.07	45	244.47	8.84 ± 0.11	2.00 ± 0.26	36.2 ± 6.2
22	t-CH ₃ CH ₂ OH	18 _{5,14} – 18 _{4,15}	232.035	-4.09	37	175.24	9.77 ± 0.22	3.28 ± 0.55	63.5 ± 13.8
23	t-CH ₃ CH ₂ OH ^{b,c}	15 _{5,10} – 15 _{4,11}	232.075	-4.15	31	132.29
32	t-CH ₃ CH ₂ OH ^c	23 _{5,19} – 23 _{4,20}	232.318	-4.07	47	263.91	8.07 ± 0.34	3.50 ± 0.89	51.8 ± 16.2
34	t-CH ₃ CH ₂ OH	17 _{5,13} – 17 _{4,14}	232.405	-4.10	35	160.07	9.23 ± 0.19	2.53 ± 0.48	38.2 ± 9.4
37	g-CH ₃ CH ₂ OH	14 _{0,14} – 13 _{0,13}	232.491	-3.95	29	141.75	8.61 ± 0.21	4.07 ± 0.52	67.9 ± 11.2
39	g-CH ₃ CH ₂ OH ^b	14 _{1,14} – 13 _{1,13}	232.597	-3.95	29	146.54
46	t-CH ₃ CH ₂ OH	16 _{5,12} – 16 _{4,13}	232.809	-4.10	33	145.73	8.98 ± 0.44	3.50 ± 1.10	36.3 ± 14.9
49	t-CH ₃ CH ₂ OH	14 _{5,9} – 14 _{4,10}	232.928	-4.12	29	119.63	8.66 ± 0.30	3.55	56.5 ± 8.5
59	g-CH ₃ CH ₂ OH	20 _{4,17} – 20 _{3,17}	233.096	-4.83	41	256.10	8.04 ± 0.24	3.09 ± 0.70	49.0 ± 14.1
81	g-CH ₃ CH ₂ OH	14 _{4,11} – 13 _{4,10}	243.120	-3.91	29	163.70	8.38 ± 0.18	2.63 ± 0.44	40.7 ± 9.0
83	g-CH ₃ CH ₂ OH ^c	14 _{4,10} – 13 _{4,9}	243.207	-3.94	29	168.57	9.03 ± 0.18	2.88 ± 0.45	59.2 ± 11.3
88	g-CH ₃ CH ₂ OH	14 _{4,10} – 13 _{4,9}	243.350	-3.91	29	163.73	9.23 ± 0.24	3.76 ± 0.60	73.9 ± 15.5
93	t-CH ₃ CH ₂ OH*	8 _{2,6} – 7 _{1,7}	243.557	-4.23	17	35.57
122	g-CH ₃ CH ₂ OH	14 _{1,13} – 13 _{1,12}	244.634	-3.84	29	151.72	8.98 ± 0.17	3.33 ± 0.42	70.4 ± 11.7
86	CH ₃ COCH ₃	19 _{6,13} – 18 _{7,12}	243.286	-3.36	624	133.29	8.15 ± 0.23	3.71 ± 0.57	(61.2 ± 12.1)/2
86	CH ₃ COCH ₃	19 _{7,13} – 18 _{6,12}	243.286	-3.36	624	133.29	8.15 ± 0.23	3.71 ± 0.57	(61.2 ± 12.1)/2
109	CH ₃ COCH ₃	20 _{5,15} – 19 _{6,14}	244.286	-3.30	656	139.46	9.07 ± 0.25	3.30 ± 0.60	(55.6 ± 13.3)/2
109	CH ₃ COCH ₃	20 _{6,15} – 19 _{5,14}	244.286	-3.30	656	139.46	9.07 ± 0.25	3.30 ± 0.60	(55.6 ± 13.3)/2

^aPartially blended with a transition from a different species. ^bCompletely blended with a transition from a different species. ^cPartially blended with an unidentified (U) transition.

Gaussian fits were not performed for completely blended lines or lines observed with SNR < 3. A FWHM with no uncertainties indicates that a fixed linewidth was adopted for the fit (Appendix B).

Table 5. Identified CH_3OCH_3 and CH_3OCHO transitions toward the continuum peak of Ser-emb 11 W. Tentative detections are indicated with a *. Integrated intensity maps of boldfaced transitions are presented in Fig. 4.

Line ID	Molecule	Transition	Frequency (GHz)	$\log_{10}(A_{ul})$ (s^{-1})	g_{up}	E_{up} (K)	V_{LSR} (km s^{-1})	FWHM	Integrated Intensity ($\text{mJy beam}^{-1} \text{ km s}^{-1}$)
20	$\text{CH}_3\text{OCH}_3^b$	13 _{0,13} – 12 _{1,12} (0)	231.988	-4.04	270	80.92
20	$\text{CH}_3\text{OCH}_3^b$	13 _{0,13} – 12 _{1,12} (1)	231.988	-4.04	432	80.92
20	$\text{CH}_3\text{OCH}_3^b$	13 _{0,13} – 12 _{1,12} (5)	231.988	-4.04	162	80.92
20	$\text{CH}_3\text{OCH}_3^b$	13 _{0,13} – 12 _{1,12} (3)	231.988	-4.04	108	80.92
62	$\text{CH}_3\text{OCH}_3^b$	22 _{2,21} – 21 _{1,22} (5)	233.189	-4.56	270	232.92
62	$\text{CH}_3\text{OCH}_3^b$	22 _{2,21} – 21 _{1,22} (3)	233.189	-4.56	180	232.92
63	CH_3OCH_3	22 _{2,21} – 21 _{1,22} (1)	233.193	-4.56	720	232.92	7.80 ± 0.07	2.08 ± 0.18	88.9 ± 10.1
64	CH_3OCH_3	22 _{2,21} – 21 _{1,22} (0)	233.198	-4.56	450	232.92	9.15 ± 0.13	2.07	50.2 ± 6.8
95	CH_3OCH_3	23_{5,18} – 23_{4,19} (5)	243.739	-4.10	282	286.98	8.49 ± 0.07	4.01 ± 0.16	$(313.0 \pm 16.4) \times 282/1692$
95	CH_3OCH_3	23_{5,18} – 23_{4,19} (3)	243.739	-4.10	188	286.98	8.49 ± 0.07	4.01 ± 0.16	$(313.0 \pm 16.4) \times 188/1692$
95	CH_3OCH_3	23_{5,18} – 23_{4,19} (1)	243.740	-4.10	752	286.98	8.49 ± 0.07	4.01 ± 0.16	$(313.0 \pm 16.4) \times 752/1692$
95	CH_3OCH_3	23_{5,18} – 23_{4,19} (0)	243.741	-4.10	470	286.98	8.49 ± 0.07	4.01 ± 0.16	$(313.0 \pm 16.4) \times 470/1692$
115	CH_3OCH_3	23 _{2,22} – 23 _{1,23} (5)	244.503	-4.31	94	253.35	8.13 ± 0.09	2.91 ± 0.23	$(81.8 \pm 8.4) \times 94/282$
115	CH_3OCH_3	23 _{2,22} – 23 _{1,23} (3)	244.503	-4.31	188	253.35	8.13 ± 0.09	2.91 ± 0.23	$(81.8 \pm 8.4) \times 188/282$
116	CH_3OCH_3	23 _{2,22} – 23 _{1,23} (1)	244.508	-4.31	752	253.35	8.23 ± 0.07	2.05 ± 0.16	74.3 ± 7.5
117	CH_3OCH_3	23 _{2,22} – 23 _{1,23} (0)	244.513	-4.31	282	253.35	8.68 ± 0.18	2.71 ± 0.45	41.4 ± 8.9
38	CH_3OCHO	19 _{9,11} – 19 _{8,12} E	232.579	-4.82	78	165.98	8.04 ± 0.17	3.31 ± 0.42	62.7 ± 10.5
39	CH_3OCHO^b	19 _{9,10} – 19 _{8,11} E	232.597	-4.82	78	165.98
40	CH_3OCHO^*	19 _{9,10} – 19 _{8,11} A	232.617	-4.82	78	165.97
41	CH_3OCHO	19 _{9,11} – 19 _{8,12} A	232.625	-4.82	78	165.97	8.71 ± 0.11	2.33 ± 0.28	61.7 ± 9.8
61	CH_3OCHO	18 _{9,9} – 18 _{8,10} A	233.166	-4.83	74	154.72
61	CH_3OCHO	19 _{18,1} – 18 _{18,0} A	233.167	-4.71	78	326.91
61	CH_3OCHO	19 _{18,2} – 18 _{18,1} A	233.167	-4.71	78	326.91
62	CH_3OCHO^b	19 _{18,2} – 18 _{18,1} E	233.189	-4.71	78	326.90
65	CH_3OCHO^a	19 _{17,2} – 18 _{17,1} A	233.200	-4.42	78	303.72	7.76 ± 0.10	2.06 ± 0.29	$(52.3 \pm 8.9)/2$
65	CH_3OCHO^a	19 _{17,3} – 18 _{17,2} A	233.200	-4.42	78	303.72	7.76 ± 0.10	2.06 ± 0.29	$(52.3 \pm 8.9)/2$
67	CH_3OCHO^a	19 _{17,2} – 18 _{17,1} E	233.213	-4.42	78	303.71
67	CH_3OCHO^a	19 _{4,16} – 18 _{4,15} E	233.213	-3.74	78	123.26
68	CH_3OCHO	19 _{17,3} – 18 _{17,2} E	233.222	-4.42	78	303.70	7.83 ± 0.16	2.68 ± 0.43	51.6 ± 10.6
69	CH_3OCHO	19 _{4,16} – 18 _{4,15} A	233.227	-3.74	78	123.25	8.66 ± 0.04	2.94 ± 0.10	225.3 ± 9.6
70	CH_3OCHO	19 _{16,3} – 18 _{16,2} A	233.246	-4.25	78	281.85	7.14 ± 0.06	2.06 ± 0.16	$(80.6 \pm 8.1)/2$
70	CH_3OCHO	19 _{16,4} – 18 _{16,3} A	233.246	-4.25	78	281.85	7.14 ± 0.06	2.06 ± 0.16	$(80.6 \pm 8.1)/2$
71	CH_3OCHO^c	19 _{16,3} – 18 _{16,2} E	233.256	-4.25	78	281.84	8.09 ± 0.24	2.78	55.2 ± 7.9
72	CH_3OCHO^c	19 _{16,4} – 18 _{16,3} E	233.269	-4.25	78	281.83	8.33 ± 0.19	2.56 ± 0.40	56.5 ± 10.9
73	CH_3OCHO	19 _{15,4} – 18 _{15,3} A	233.310	-4.14	78	261.30	8.15 ± 0.07	2.53 ± 0.16	$(112.6 \pm 9.6)/2$
73	CH_3OCHO	19 _{15,5} – 18 _{15,4} A	233.310	-4.14	78	261.30	8.15 ± 0.07	2.53 ± 0.16	$(112.6 \pm 9.6)/2$
74	CH_3OCHO	19 _{15,4} – 18 _{15,3} E	233.316	-4.14	78	261.29	8.46 ± 0.08	2.09 ± 0.18	66.7 ± 7.7
75	CH_3OCHO	19 _{15,5} – 18 _{15,4} E	233.331	-4.14	78	261.28	7.65 ± 0.25	2.78	54.0 ± 8.6
114	CH_3OCHO^b	32 _{10,22} – 32 _{9,23} A	244.490	-4.66	130	379.67
119	CH_3OCHO	20 _{4,17} – 19 _{4,16} E	244.580	-3.68	82	134.99	8.20 ± 0.04	2.62 ± 0.11	217.1 ± 12.3
121	CH_3OCHO^a	20 _{4,17} – 19 _{4,16} A	244.594	-3.68	82	134.98	8.48 ± 0.04	2.67 ± 0.11	213.7 ± 11.0

^aPartially blended with a transition from a different species. ^bCompletely blended with a transition from a different species. ^cPartially blended with an unidentified (U) transition.

Gaussian fits were not performed for completely blended lines or lines observed with $\text{SNR} < 3$. A FWHM with no uncertainties indicates that a fixed linewidth was adopted for the fit (Appendix B).

Table 6. Identified CH₃OCHO $\nu=1$ transitions toward the continuum peak of Ser-emb 11 W in the 231.262 – 233.380 GHz range.

Line ID	Molecule	Transition	Frequency (GHz)	$\log_{10}(A_{ul})$ (s ⁻¹)	g_{up}	E_{up} (K)	V_{LSR} (km s ⁻¹)	FWHM	Integrated Intensity (mJy beam ⁻¹ km s ⁻¹)
4	CH ₃ OCHO $\nu=1$	18 _{4,14} – 17 _{4,13} E	231.724	-3.75	74	300.80	8.27 ± 0.05	2.45 ± 0.13	134.8 ± 9.3
5	CH ₃ OCHO ^b $\nu=1$	19 _{14,6} – 18 _{14,5} E	231.735	-4.06	78	429.95
6	CH ₃ OCHO ^c $\nu=1$	19 _{10,9} – 18 _{10,8} E	231.749	-3.87	78	366.05	8.09 ± 0.16	2.78	48.6 ± 7.2
8	CH ₃ OCHO $\nu=1$	19 _{16,3} – 18 _{16,2} A	231.801	-4.26	78	469.99
8	CH ₃ OCHO $\nu=1$	19 _{16,4} – 18 _{16,3} A	231.801	-4.26	78	469.99
8	CH ₃ OCHO $\nu=1$	19 _{17,2} – 18 _{17,1} A	231.802	-4.24	78	492.08
8	CH ₃ OCHO $\nu=1$	19 _{17,3} – 18 _{17,2} A	231.802	-4.24	78	492.08
8	CH ₃ OCHO $\nu=1$	19 _{18,1} – 18 _{18,0} A	231.803	-4.71	78	515.51
8	CH ₃ OCHO $\nu=1$	19 _{18,2} – 18 _{18,1} A	231.803	-4.71	78	515.51
8	CH ₃ OCHO $\nu=1$	24 _{9,15} – 24 _{8,16} E	231.804	-4.78	98	418.01
8	CH ₃ OCHO $\nu=1$	19 _{15,4} – 18 _{15,3} A	231.804	-4.15	78	449.25
8	CH ₃ OCHO $\nu=1$	19 _{15,5} – 18 _{15,4} A	231.804	-4.15	78	449.25
9	CH ₃ OCHO $\nu=1$	19 _{14,5} – 18 _{14,4} A	231.817	-4.06	78	429.85	8.62 ± 0.17	2.78	(60.2 ± 7.0)/2
9	CH ₃ OCHO $\nu=1$	19 _{14,6} – 18 _{14,5} A	231.817	-4.06	78	429.85	8.62 ± 0.17	2.78	(60.2 ± 7.0)/2
11	CH ₃ OCHO $\nu=1$	19 _{13,6} – 18 _{13,5} A	231.847	-4.00	78	411.79	8.59 ± 0.09	2.68 ± 0.23	(87.1 ± 9.6)/2
11	CH ₃ OCHO $\nu=1$	19 _{13,7} – 18 _{13,6} A	231.847	-4.00	78	411.79	8.59 ± 0.09	2.68 ± 0.23	(87.1 ± 9.6)/2
14	CH ₃ OCHO $\nu=1$	19 _{4,16} – 18 _{4,15} E	231.896	-3.75	78	309.75	8.24 ± 0.08	2.46 ± 0.18	118.8 ± 10.8
15	CH ₃ OCHO ^b $\nu=1$	19 _{12,7} – 18 _{12,6} A	231.904	-3.95	78	395.09
15	CH ₃ OCHO ^b $\nu=1$	19 _{12,8} – 18 _{12,7} A	231.904	-3.95	78	395.09
21	CH ₃ OCHO ^c $\nu=1$	19 _{11,8} – 18 _{11,7} A	232.003	-3.90	78	397.73	9.03 ± 0.11	2.99 ± 0.28	(103.4 ± 12.4)/2
21	CH ₃ OCHO ^c $\nu=1$	19 _{12,8} – 18 _{12,7} A	232.003	-3.90	78	397.73	9.03 ± 0.11	2.99 ± 0.28	(103.4 ± 12.4)/2
25	CH ₃ OCHO ^a $\nu=1$	19 _{9,10} – 18 _{9,9} E	232.160	-3.83	78	353.32	7.98 ± 0.14	2.78	74.9 ± 6.7
26	CH ₃ OCHO ^b $\nu=1$	19 _{10,9} – 18 _{10,8} A	232.164	-3.86	78	365.73
26	CH ₃ OCHO ^b $\nu=1$	19 _{10,10} – 18 _{10,9} A	232.164	-3.86	78	365.73
33	CH ₃ OCHO $\nu=1$	19 _{11,9} – 18 _{11,8} E	232.378	-3.90	78	379.55	9.38 ± 0.14	2.11 ± 0.35	35.2 ± 7.6
36	CH ₃ OCHO ^a $\nu=1$	19 _{9,10} – 18 _{9,9} A	232.423	-3.83	78	353.09	8.39 ± 0.11	2.70 ± 0.27	(122.9 ± 16.0)/2
36	CH ₃ OCHO ^a $\nu=1$	19 _{9,11} – 18 _{9,10} A	232.423	-3.83	78	353.09	8.39 ± 0.11	2.70 ± 0.27	(122.9 ± 16.0)/2
42	CH ₃ OCHO $\nu=1$	19 _{10,10} – 18 _{10,9} E	232.684	-3.86	78	365.47	8.69 ± 0.10	2.18 ± 0.24	66.1 ± 9.6
43	CH ₃ OCHO $\nu=1$	19 _{8,11} – 18 _{8,10} E	232.739	-3.80	78	341.98	9.04 ± 0.14	2.19 ± 0.34	49.4 ± 10.1
47	CH ₃ OCHO $\nu=1$	19 _{8,12} – 18 _{8,11} A	232.836	-3.80	78	341.83	8.29 ± 0.13	2.78	64.8 ± 5.5
48	CH ₃ OCHO $\nu=1$	19 _{8,11} – 18 _{8,10} A	232.840	-3.80	78	341.83	8.99 ± 0.08	2.53 ± 0.20	73.6 ± 7.7
57	CH ₃ OCHO ^c $\nu=1$	19 _{9,11} – 18 _{9,10} E	233.080	-3.83	78	352.77

^aPartially blended with a transition from a different species. ^bCompletely blended with a transition from a different species. ^cPartially blended with an unidentified (U) transition.

Gaussian fits were not performed for completely blended lines or lines observed with SNR < 3. A FWHM with no uncertainties indicates that a fixed linewidth was adopted for the fit (Appendix B).

an iterative process is needed in order to derive the T_{rot} and N_{tot} values from Eq. C7. In this work we have used the affine-invariant MCMC package `emcee` (Foreman-Mackey et al. 2013) to find the COM excitation temperatures and column densities that best fit the observations (i.e., the 50th percentile from the posteriors). Ad-

ditional information on the MCMC fitting can be found in (Loomis et al. 2018) and Bergner et al. (2019).

D. ROTATIONAL TEMPERATURES AND COLUMN DENSITIES ESTIMATED WITH THE MADCUBA PACKAGE

The `Autofit` function of the SLIM tool within the MADCUBA package was used to perform a non-linear

Table 7. Identified CH₃OCHO $\nu=1$ transitions toward the continuum peak of Ser-emb 11 W in the 242.978 – 244.853 GHz range. Tentative detections are indicated with a *.

Line	Molecule	Transition	Frequency (GHz)	$\log(A_{ul})$ (s ⁻¹)	g_{up}	E_{up} (K)	V_{LSR} (km s ⁻¹)	FWHM	Integrated Intensity (mJy beam ⁻¹ km s ⁻¹)
79	CH ₃ OCHO ^a	$\nu=1$ 20 _{16,4} – 19 _{16,3} E	243.057	-4.11	82	482.38	8.51 ± 0.29	2.78	33.6 ± 6.4
85	CH ₃ OCHO ^b	$\nu=1$ 20 _{4,17} – 19 _{4,16} E	243.223	-3.68	82	321.42
87	CH ₃ OCHO*	$\nu=1$ 20 _{13,7} – 19 _{13,6} E	243.325	-3.90	82	424.03
91	CH ₃ OCHO ^c	$\nu=1$ 20 _{12,8} – 19 _{12,7} E	243.511	-3.85	82	407.25	7.87 ± 0.20	2.78	64.7 ± 7.1
96	CH ₃ OCHO ^b	$\nu=1$ 20 _{11,9} – 19 _{11,8} E	243.766	-3.82	82	391.83	7.60 ± 0.12	3.88 ± 0.29	131.4 ± 12.9
99	CH ₃ OCHO*	$\nu=1$ 20 _{14,7} – 19 _{14,6} E	244.000	-3.95	82	441.66
100	CH ₃ OCHO ^b	$\nu=1$ 20 _{15,5} – 19 _{15,4} E	244.048	-4.02	82	460.96
100	CH ₃ OCHO ^b	$\nu=1$ 20 _{15,6} – 19 _{15,5} E	244.048	-4.02	82	460.96
101	CH ₃ OCHO $\nu=1$	19 _{4,15} – 18 _{4,14} A	244.067	-3.68	78	312.75	8.92 ± 0.06	2.14 ± 0.15	97.7 ± 9.1
102	CH ₃ OCHO $\nu=1$	20 _{14,6} – 19 _{14,5} A	244.074	-3.95	82	441.56	8.79 ± 0.21	2.78	(49.5 ± 7.1)/2
102	CH ₃ OCHO $\nu=1$	20 _{14,7} – 19 _{14,6} A	244.074	-3.95	82	441.56	8.79 ± 0.21	2.78	(49.5 ± 7.1)/2
103	CH ₃ OCHO $\nu=1$	20 _{10,10} – 19 _{10,9} E	244.112	-3.78	82	377.76	8.19 ± 0.16	3.92 ± 0.38	97.6 ± 12.5
104	CH ₃ OCHO $\nu=1$	20 _{13,7} – 19 _{13,6} A	244.120	-3.90	82	423.51	8.55 ± 0.13	3.68 ± 0.32	(92.1 ± 10.5)/2
104	CH ₃ OCHO $\nu=1$	20 _{13,8} – 19 _{13,7} A	244.120	-3.90	82	423.51	8.55 ± 0.13	3.68 ± 0.32	(92.1 ± 10.5)/2
106	CH ₃ OCHO $\nu=1$	20 _{12,8} – 19 _{12,7} A	244.198	-3.85	82	406.81	8.27 ± 0.16	2.78	(81.9 ± 8.5)/2
106	CH ₃ OCHO $\nu=1$	20 _{12,9} – 19 _{12,8} A	244.198	-3.85	82	406.81	8.27 ± 0.16	2.78	(81.9 ± 8.5)/2
107	CH ₃ OCHO*	$\nu=1$ 20 _{13,8} – 19 _{13,7} E	244.207	-3.89	82	423.51
110	CH ₃ OCHO ^a	$\nu=1$ 20 _{11,9} – 19 _{11,8} A	244.326	-3.81	82	391.46	8.11 ± 0.19	2.78	(112.5 ± 12.9)/2
110	CH ₃ OCHO ^a	$\nu=1$ 20 _{11,10} – 19 _{11,9} A	244.326	-3.81	82	391.46	8.11 ± 0.19	2.78	(112.5 ± 12.9)/2
113	CH ₃ OCHO*	$\nu=1$ 20 _{12,9} – 19 _{12,8} E	244.446	-3.85	82	406.72
118	CH ₃ OCHO $\nu=1$	20 _{10,10} – 19 _{10,9} A	244.529	-3.78	82	377.46	9.08 ± 0.09	1.87 ± 0.21	(62.0 ± 9.1)/2
118	CH ₃ OCHO $\nu=1$	20 _{10,11} – 19 _{10,10} A	244.529	-3.78	82	377.46	9.08 ± 0.09	1.87 ± 0.21	(62.0 ± 9.1)/2
120	CH ₃ OCHO ^b	$\nu=1$ 20 _{9,11} – 19 _{9,10} E	244.588	-3.75	82	365.06
124	CH ₃ OCHO $\nu=1$	20 _{11,10} – 19 _{11,9} E	244.730	-3.81	82	391.29	8.57 ± 0.13	2.78	72.1 ± 6.2
127	CH ₃ OCHO ^a	$\nu=1$ 20 _{9,11} – 19 _{9,10} A	244.845	-3.75	82	364.84	7.90 ± 0.09	2.30 ± 0.25	(79.8 ± 11.0)/2
127	CH ₃ OCHO ^a	$\nu=1$ 20 _{9,12} – 19 _{9,11} A	244.845	-3.75	82	364.84	7.90 ± 0.09	2.30 ± 0.25	(79.8 ± 11.0)/2

^aPartially blended with a transition from a different species. ^bCompletely blended with a transition from a different species. ^cPartially blended with an unidentified (U) transition.

Gaussian fits were not performed for completely blended lines or lines observed with SNR < 3. A FWHM with no uncertainties indicates that a fixed linewidth was adopted for the fit (Appendix B).

least-squares fit of a synthetic LTE spectrum to the observed spectrum (Martín et al. 2019). We used the values derived from the population diagram analysis (Table 2) as the initial parameters of the fit, with a fixed line FWHM according to the values reported in Sect. 3.4, and a fixed source size of 0.14". The best-fit rotational temperatures and column densities are listed in Table 10 and were used to cross-check those presented in Table 2. We note that even though the fit did not converge for C₂H₅OH, CH₃COCH₃, NH₂CHO, and ¹³CH₃CN, the simulated spectrum assuming the values in Table 2 was consistent with the observations. Similar excitation temperatures were found, within a 35% difference,

for CH₃OH, CH₂DOH, and CH₃OCH₃, while they were the same, within errors, for the N-bearing COMs. In the cases of CH₃OCH₃ and CH₃OCHO, the estimated temperatures were consistent, within errors, with the temperatures found for CH₃OH and CH₂DOH through the MCMC fitting of the population diagrams. In Sect. 3.4 we explain that the CH₃OCH₃ rotational temperature calculated with the population diagram analysis could have been overestimated. The derived column densities for the O-bearing COMs were within a factor of 2 compared to those reported in Table 2, and the resulting column density ratios were near identical except for CH₃OCH₃, with a 35% higher abundance with respect

Table 8. Identified N-bearing COM transitions toward the continuum peak of Ser-emb 11 W. Tentative detections are indicated with a * Integrated maps of boldfaced transitions are presented in Fig. 4.

Line ID	Molecule	Transition	Frequency (GHz)	$\log_{10}(A_{ul})$ (s^{-1})	g_{up}	E_{up} (K)	V_{LSR} ($km\ s^{-1}$)	FWHM	Integrated Intensity ($mJy\ beam^{-1}\ km\ s^{-1}$)
13	HNCO*	28 _{1,28,27} – 29 _{0,29,28}	231.873	-4.18	55	469.87	9.18 ± 0.20	4.86 ± 0.49	(141.6 ± 18.5) x 55/171
13	HNCO*	28 _{1,28,29} – 29 _{0,29,30}	231.873	-4.18	59	469.87	9.18 ± 0.20	4.86 ± 0.49	(141.6 ± 18.5) x 59/171
13	HNCO*	28 _{1,28,28} – 29 _{0,29,29}	231.873	-4.18	57	469.87	9.18 ± 0.20	4.86 ± 0.49	(141.6 ± 18.5) x 57/171
31	NH ₂ CHO ^c	11 _{2,10} – 10 _{2,9}	232.274	-3.05	23	78.93	10.28 ± 0.36	3.50 ± 0.82	89.9 ± 23.6
92	NH₂CHO^c	12_{1,12} – 11_{1,11}	243.521	-2.98	25	79.17	10.30 ± 0.69	5.19 ± 1.14	178.4 ± 43.1
76	CH ₂ DCN	14 _{5,9} – 13 _{5,8}	243.013	-2.97	29	222.27	8.27 ± 0.15	3.27 ± 0.35	(80.4 ± 11.4)/2
76	CH ₂ DCN	14 _{5,10} – 13 _{5,9}	243.013	-2.97	29	222.27	8.27 ± 0.15	3.27 ± 0.35	(80.4 ± 11.4)/2
77	CH ₂ DCN	14 _{0,14} – 13 _{0,13}	243.041	-2.91	29	87.50	8.27 ± 0.12	3.63 ± 0.30	123.9 ± 13.4
78	CH ₂ DCN	14 _{4,10} – 13 _{4,9}	243.051	-2.94	29	173.77	7.78 ± 0.10	3.46 ± 0.25	(142.2 ± 13.4)/2
78	CH ₂ DCN	14 _{4,11} – 13 _{4,10}	243.051	-2.94	29	173.77	7.78 ± 0.10	3.46 ± 0.25	(142.2 ± 13.4)/2
80	CH₂DCN	14_{3,12} – 13_{3,11}	243.083	-2.93	29	136.04
80	CH₂DCN	14_{2,13} – 13_{2,12}	243.083	-2.92	29	109.08
80	CH₂DCN	14_{3,11} – 13_{3,10}	243.083	-2.93	29	136.04
82	CH ₂ DCN	14 _{2,12} – 13 _{2,11}	243.152	-2.92	29	109.09	8.59 ± 0.10	2.52 ± 0.23	94.7 ± 11.5
105	CH ₂ DCN	14 _{1,13} – 13 _{1,12}	244.143	-2.90	29	93.28	8.65 ± 0.12	3.36 ± 0.29	125.2 ± 14.1
23	¹³ CH ₃ CN ^{b,c}	13 ₆ – 12 ₆	232.077	-3.07	108	355.51
24	¹³ CH ₃ CN* ^c	13 ₅ – 12 ₅	232.125	-3.04	54	256.88
26	¹³ CH ₃ CN ^b	13 ₄ – 12 ₄	232.164	-3.01	54	192.51
27	¹³CH₃CN	13₃ – 12₃	232.195	-2.99	108	142.43	8.50 ± 0.11	2.94 ± 0.27	92.5 ± 11.1
28	¹³ CH ₃ CN	13 ₂ – 12 ₂	232.216	-2.98	54	106.65	7.35 ± 0.11	2.74 ± 0.28	79.0 ± 10.5
29	¹³ CH ₃ CN	13 ₁ – 12 ₁	232.230	-2.97	54	85.18	8.53 ± 0.10	3.51 ± 0.25	93.6 ± 8.6
30	¹³ CH ₃ CN	13 ₀ – 12 ₀	232.234	-2.97	54	78.02	8.41 ± 0.09	2.73 ± 0.21	82.5 ± 8.2
15	CH ₃ C ¹⁵ N ^b	13 ₃ – 12 ₃	231.902	-2.99	108	142.34
16	CH ₃ C ¹⁵ N	13 ₂ – 12 ₂	231.924	-2.98	54	106.55	7.82 ± 0.16	3.08 ± 0.40	50.8 ± 8.7
17	CH₃C¹⁵N	13₁ – 12₁	231.937	-2.97	54	85.08	6.65 ± 0.12	3.08	76.6 ± 5.0
18	CH ₃ C ¹⁵ N	13 ₀ – 12 ₀	231.941	-2.97	54	77.93	7.76 ± 0.18	3.08	50.1 ± 5.0
12	CH₃CH₂CN	27_{1,27} – 26_{1,26}	231.854	-2.98	55	157.73	8.16 ± 0.10	3.46 ± 0.26	94.1 ± 9.0
20	CH ₃ CH ₂ CN ^b	27 _{0,27} – 26 _{0,26}	231.990	-2.98	55	157.71
45	CH ₃ CH ₂ CN	26 _{3,24} – 25 _{3,23}	232.790	-2.98	53	161.02	8.78 ± 0.24	3.45 ± 0.64	64.7 ± 15.3
51	CH ₃ CH ₂ CN	26 _{10,16} – 25 _{10,15}	232.962	-3.04	53	261.96	7.91 ± 0.13	2.12 ± 0.31	(40.5 ± 7.8)/2
51	CH ₃ CH ₂ CN	26 _{10,17} – 25 _{10,16}	232.962	-3.04	53	261.96	7.91 ± 0.13	2.12 ± 0.31	(40.5 ± 7.8)/2
52	CH ₃ CH ₂ CN	26 _{9,17} – 25 _{9,16}	232.968	-3.03	53	240.89	9.19 ± 0.14	2.72 ± 0.34	(51.9 ± 8.5)/2
52	CH ₃ CH ₂ CN	26 _{9,18} – 25 _{9,17}	232.968	-3.03	53	240.89	9.19 ± 0.14	2.72 ± 0.34	(51.9 ± 8.5)/2
53	CH ₃ CH ₂ CN	26 _{11,15} – 25 _{11,14}	232.976	-3.06	53	285.23	8.92 ± 0.19	3.59 ± 0.47	(57.5 ± 9.7)/2
53	CH ₃ CH ₂ CN	26 _{11,16} – 25 _{11,15}	232.976	-3.06	53	285.23	8.92 ± 0.19	3.59 ± 0.47	(57.5 ± 9.7)/2
54	CH ₃ CH ₂ CN	26 _{8,18} – 25 _{8,17}	232.999	-3.01	53	222.04	9.68 ± 0.16	3.28 ± 0.43	(65.4 ± 11.2)/2
54	CH ₃ CH ₂ CN	26 _{8,19} – 25 _{8,18}	232.999	-3.01	53	222.04	9.68 ± 0.16	3.28 ± 0.43	(65.4 ± 11.2)/2
55	CH ₃ CH ₂ CN	26 _{12,14} – 25 _{12,13}	233.003	-3.07	53	310.69	8.26 ± 0.23	3.18 ± 0.57	(44.8 ± 10.5)/2
55	CH ₃ CH ₂ CN	26 _{12,15} – 25 _{12,14}	233.003	-3.07	53	310.69	8.26 ± 0.23	3.18 ± 0.57	(44.8 ± 10.5)/2
56	CH ₃ CH ₂ CN	26 _{7,19} – 25 _{7,18}	233.069	-3.00	53	205.40	8.47 ± 0.19	3.61 ± 0.47	(101.4 ± 17.2)/2
56	CH ₃ CH ₂ CN	26 _{7,20} – 25 _{7,19}	233.069	-3.00	53	205.40	8.47 ± 0.19	3.61 ± 0.47	(101.4 ± 17.2)/2
58	CH ₃ CH ₂ CN ^c	26 _{14,12} – 25 _{14,11}	233.089	-3.12	53	368.17
58	CH ₃ CH ₂ CN ^c	26 _{14,13} – 25 _{14,12}	233.089	-3.12	53	368.17
94	CH ₃ CH ₂ CN	27 _{4,23} – 26 _{4,22}	243.643	-2.92	55	180.79	7.58 ± 0.18	3.34 ± 0.43	80.5 ± 13.7

^aPartially blended with a transition from a different species. ^bCompletely blended with a transition from a different species. ^cPartially blended with an unidentified (U) transition.

Gaussian fits were not performed for completely blended lines or lines observed with SNR < 3. A FWHM with no uncertainties indicates that a fixed linewidth was adopted for the fit (Appendix B).

Table 9. Identified transitions corresponding to small molecules (4 atoms or less) detected toward the continuum peak of Ser-emb 11 W.

Line ID	Molecule	Transition	Frequency (GHz)	$\log_{10}(A_{ul})$ (s^{-1})	g_{up}	E_{up} (K)	V_{LSR} ($km\ s^{-1}$)	FWHM	Integrated Intensity ($mJy\ beam^{-1}\ km\ s^{-1}$)
	CO ^a	2 – 1	230.538	-6.16	5	16.60	~12.6	~17.7	≥11360
	¹³ CO ^a	2 – 1	220.399	-6.22	5	15.87	~8.1	~5.2	≥1380
	C ¹⁸ O ^a	2 – 1	219.560	-6.22	5	15.81	~7.9	~2.0	≥380
	H ₂ CO ^a	3 _{0,3} – 2 _{0,2}	218.222	-3.55	7	20.96	~8.5	~3.5	≥920
	H ₂ CO	3 _{2,2} – 2 _{2,1}	218.476	-3.80	7	68.09	9.33 ± 0.04	3.53 ± 0.10	506.8 ± 18.7
	HDCO	4 _{2,2} – 3 _{2,1}	259.035	-3.43	9	62.86	8.25 ± 0.11	3.91 ± 0.31	230.2 ± 23.0
	DCN	3 – 2	217.238	-3.49	33	20.85	8.44 ± 0.09	4.22 ± 0.21	291.9 ± 19.1
	H ¹³ CN ^a	3 ₂ – 2 ₂	259.012	-3.34	33	24.86	~8.7	~6.1	≥1000
	HC ¹⁵ N	3 – 2	258.157	-3.09	7	24.78	8.52 ± 0.09	4.09 ± 0.24	409.3 ± 30.0
108	SO ₂	14 _{0,14} – 13 _{1,13}	244.254	-3.79	29	93.90	8.77 ± 0.09	6.47 ± 0.23	554.6 ± 25.9
	SO ₂	11 _{3,9} – 11 _{2,10}	262.257	-3.85	23	82.80	8.79 ± 0.14	4.28 ± 0.41	276.4 ± 32.8
	CS ^a	5 – 4	244.936	-3.52	11	35.27	~9.3	~4.0	≥1740
100	H ₂ CS ^b	7 _{1,6} – 6 _{1,5}	244.048	-3.68	45	60.04	8.13 ± 0.05	3.22 ± 0.11	<i>459.9 ± 20.9</i>
84	OCS ^b	20 – 19	243.218	-4.38	41	122.57	8.55 ± 0.03	2.98 ± 0.09	692.1 ± 25.9
	O ¹³ CS	18 – 17	218.199	-4.52	37	99.49	8.34 ± 0.05	2.25 ± 0.11	178.5 ± 11.4

^aThe self-absorption of the emission line prevents us from properly calculating its position, width or integrated intensity. Only an approximate lower limit is indicated in this case, calculated from the Gaussian fit of the emission line without taking into account the channels affected by the self-absorption. ^bBlended with a transition from a different species.

For blended emission lines, a Gaussian deconvolution was performed in order to estimate the integrated intensity of the different components. Values in italics indicate that contribution from neighboring lines could not be ruled out.

Table 10. COM column densities and rotational temperatures in the hot corino of Ser-emb 11 W. Values are estimated from a Gaussian fit of the observed spectrum using the MADCUBA software assuming a circular source with size $\Omega_{source} = 0.14''$.

Molecule	T_{rot} (K)	N_T (cm^{-2})	$N_T/N_T(CH_3OH)$ (%)
CH ₃ OH	208 ± 4	$(1.82 ± 0.05) × 10^{18}$	100
CH ₂ DOH	115 ± 11	$(2.2 ± 0.1) × 10^{17}$	13
C ₂ H ₅ OH
CH ₃ OCH ₃	197 ± 17	$(4.6 ± 0.4) × 10^{17}$	26
CH ₃ OCHO	177 ± 6	$(2.7 ± 0.2) × 10^{17}$	15
CH ₃ COCH ₃
NH ₂ CHO
CH ₂ DCN	172 ± 46	$(2.3 ± 0.4) × 10^{15}$	0.13
¹³ CH ₃ CN
CH ₃ C ¹⁵ N	167 ± 83	$(7 ± 2) × 10^{14}$	0.04
C ₂ H ₅ CN	202 ± 88	$(4.5 ± 0.6) × 10^{15}$	0.25

NOTE—The `Autofit` function of the MADCUBA software did not converge for CH₃COCH₃, NH₂CHO, ¹³CH₃CN, and C₂H₅CN.

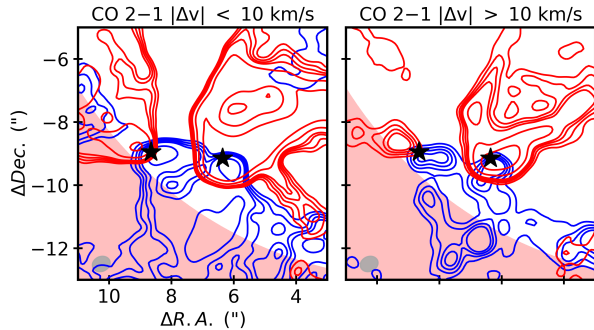


Figure 13. 6, 12, 18, 24, 48, and 96σ contours ($\sigma \sim 18$ mJy) of the low velocity ($\Delta v < 10$ km/s, left panel) and high velocity ($\Delta v > 10$ km/s, right panel) integrated redshifted and blueshifted CO 2–1 emission toward Ser-emb 11. The position of the continuum emission peaks is marked with a star symbol in each panel. The size of the synthesized beam is shown on the lower left corner of each panel. The region of the field of view observed outside the half power beam width of the primary beam is colored in red.

to CH_3OH . On the other hand, the derived column densities for CH_2DCN , $\text{CH}_3\text{C}^{15}\text{N}$, and $\text{C}_2\text{H}_5\text{CN}$ were the same, within errors, as those estimated through the population diagram analysis.

E. OUTFLOW SIGNATURE IN SER-EMB 11 W

Fig. 13 presents the integrated redshifted and blueshifted CO $J = 2-1$ emission decomposed into the low velocity ($\Delta V < 10$ km/s) and high-velocity ($\Delta V > 10$ km/s) components, in order to disentangle the higher velocity emission, more likely corresponding to the v-shaped outflow. We have used a velocity source of $V_{LSR} = 8.2$ km/s, as measured for the C^{18}O $J = 2-1$ emission in a $2''$ diameter region around the continuum peak of Ser-emb 11 W.

F. REPORTED COM COLUMN DENSITIES IN CLASS 0 AND CLASS I HOT CORINOS

Tables 11 and 12 list the column densities of a series of O- and N-bearing COMs in Class 0 and Class I hot corino sources reported in the literature, along with those found toward Ser-emb 11 W in this work. For space-saving purposes, only two significant figures are provided for most of the column density values. For the exact reported values and uncertainties, please check the corresponding references.

Table 11. Column densities (cm^{-2}) of selected O- and N-bearing COMs in Class 0 hot corinos reported in the literature

Species	16293A ^a	16293B ^b	4A2 ^c	2A ^d	HH212 ^e	B335 ^f	L483 ^g	B1-b5 ^h	Ser-emb 1 ⁱ	Ser-emb 8 ^j	BHR71 ^k	B1-c ^l	
CH ₂ CO	9.1±2.7	48	7.0	...	3.8±2.0	0.13±0.03	...	1.0±0.1	...	1.3±0.1	×10 ¹⁵
CH ₃ OH	13±4	10	10	1.2±0.4	1.3±0.7	...	17	0.50±0.06	0.12±0.04	1.4±0.6	2.4	1.9±0.6	×10 ¹⁸
CH ₂ DOH	11±3	7.1	1.6±0.7	...	4.0	...	0.48±0.18	0.60±0.07	0.7	1.6±0.1	×10 ¹⁷
¹³ CH ₃ OH	20±7	4.8±1.3	2.5±1.4	...	25	0.15±0.05	...	1.0±0.1	1.3	1.8±0.2	×10 ¹⁶
CH ₃ CHO	0.4±0.1	12	1.9	...	1.5±0.6	0.14±0.02	8.0	0.06±0.01	...	0.10±0.01	...	0.46±0.10	×10 ¹⁶
C ₂ H ₅ OH	8.0±2.4	23	4.9	5.1±2.2	2.7±1.2	0.21±0.03	10	0.30±0.02	1.3	1.5±0.3	×10 ¹⁶
CH ₃ OCH ₃	52±16	24	4.5	4.1±1.6	...	0.19±0.02	8.0	0.67±0.04	9.2±3.8	1.2±0.1	1.0	2.4±0.1	×10 ¹⁶
CH ₃ OCHO	27±8	26	3.5	6.4±1.9	3.2±1.6	0.26±0.03	13	0.38±0.02	9.1±3.6	1.6±0.2	8.1	1.9±0.1	×10 ¹⁶
CH ₃ COCH ₃	2.4±0.7	...	0.6	0.05±0.05	...	0.05±0.01	...	0.53±0.03	1.0	0.80±0.09	×10 ¹⁶
NH ₂ CHO	1.9±0.6	10	2.0	12	1.6±0.9	0.24±0.02	10	0.27±0.03	...	0.51±0.24	×10 ¹⁵
CH ₃ CN	8.0±1.0	4.0±1.0	4.8	1.0±0.2	0.29±0.10	...	0.74±0.22	×10 ¹⁶
CH ₂ DCN	3.5±0.5	1.4±0.2	0.4±0.2	0.10±0.02	...	0.26±0.02	×10 ¹⁵
¹³ CH ₃ CN	10±2	6.0±0.2	×10 ¹⁴
CH ₃ C ¹⁵ N	3.4±0.2	1.6±0.2	×10 ¹⁴
C ₂ H ₅ CN	9.0±0.2	3.6±0.2	1.5	1.2	...	0.10	1.1±0.6	...	1.1±0.3	×10 ¹⁵

NOTE—^aO-bearing COMs from Manigand et al. (2020). N-bearing COMs from Calcutt et al. (2018). ^bO-bearing COMs from Jørgensen et al. (2018). CH₃OH was derived from CH₃¹⁸O assuming a ¹⁶O/¹⁸O abundance ratio of 560 as in Wilson & Rood (1994). 20% uncertainties were assumed. N-bearing COMs from Calcutt et al. (2018). ^cFrom López-Sepulcre et al. (2017) (assuming T_{rot} = 200 K, except for CH₃OCH₃ and CH₃OCHO). CH₃OH derived from centimeter observations with the Very Large Array (VLA, De Simone et al. 2020). ^dFrom Taquet et al. (2015) (assuming T_{rot} = 179 K for NH₂CHO and C₂H₅CN). ^eFrom Lee et al. (2019). CH₃OH was derived from ¹³CH₃O assuming a ¹²C/¹³C ratio of 50 for the Orion complex as in Kahane et al. (2018). ^fFrom Imai et al. (2016) (assuming T_{rot} = 100 K). C₂H₅OH, CH₃OCH₃, CH₃OCH₃, and C₂H₅CN detections are tentative. ^gFrom Jacobsen et al. (2019). ^hFrom van Gelder et al. (2020) using Band 6 observations only. CH₃OH was derived from CH₃¹⁸O assuming a ¹⁶O/¹⁸O abundance ratio of 560 as in Wilson & Rood (1994). CH₂CO detection was considered tentative. ⁱFrom Martín-Doménech et al. (2019). ^jO-bearing COMs from van Gelder et al. (2020) using Band 6 observations only. CH₃OH was derived from CH₃¹⁸O assuming a ¹⁶O/¹⁸O abundance ratio of 560 as in Wilson & Rood (1994). CH₂CO detection was considered tentative. N-bearing COMs from Nazari et al. (2021). ^kFrom Yang et al. (2020). ^lO-bearing COMs from van Gelder et al. (2020) using Band 6 observations only. CH₃OH was derived from CH₃¹⁸O assuming a ¹⁶O/¹⁸O abundance ratio of 560 as in Wilson & Rood (1994). CH₂CO detection was considered tentative. N-bearing COMs from Nazari et al. (2021).

Table 12. Column densities (cm^{-2}) of selected O- and N-bearing COMs in Class I hot corinos reported in the literature

Species	SVS13-A ^a	L1551-IRS5 ^b	Ser-emb 17 ^c	Ser-emb 11 ^d	
CH ₂ CO	3.1 ^{+4.3} _{-2.1}	...	×10 ¹⁵
CH ₃ OH	0.81 ^{+0.50} _{-0.31}	≥10	0.28 ^{+0.01} _{-0.01}	3.7 ^{+0.4} _{-0.3}	×10 ¹⁸
CH ₂ DOH	...	≥5	...	4.4 ^{+0.4} _{-0.4}	×10 ¹⁷
CH ₃ CHO	2.5 ^{+1.7} _{-1.4}	×10 ¹⁶
C ₂ H ₅ OH	9.6 ^{+1.8} _{-3.1}	14.9±1.3	...	11.3 ^{+0.6} _{-0.6}	×10 ¹⁶
CH ₃ OCH ₃	11 ⁺² ₋₁	...	12 ⁺¹⁸ ₋₈	54 ⁺¹ ₋₁	×10 ¹⁶
CH ₃ OCHO	33 ⁺¹² ₋₆	33±2	17 ⁺³⁵ ₋₈	79 ⁺⁶ ₋₈	×10 ¹⁶
CH ₃ COCH ₃	6.3 ^{+3.7} _{-4.4}	7.1 ^{+0.8} _{-0.8}	×10 ¹⁶
NH ₂ CHO	1.9 ^{+0.6} _{-0.7}	...	1.9 ^{+2.7} _{-1.2}	3.9 ^{+0.9} _{-0.8}	×10 ¹⁵
CH ₃ CN	0.59 ^{+0.18} _{-0.13}	×10 ¹⁶
CH ₂ DCN	1.9 ^{+1.0} _{-0.8}	2.8 ^{+0.2} _{-0.1}	×10 ¹⁵
¹³ CH ₃ CN	1.23 ^{+0.08} _{-0.08}	×10 ¹⁵
CH ₃ C ¹⁵ N	8.2 ^{+0.5} _{-0.5}	×10 ¹⁴
C ₂ H ₅ CN	2.8 ^{+0.9} _{-0.6}	8.1 ^{+1.2} _{-1.0}	×10 ¹⁵

NOTE—^aFrom Yang et al. (2021). ^bFrom Bianchi et al. (2020). ^cFrom Bergner et al. (2019). ^dThis work.